VISCOUS EFFECTS IN AIRCRAFT TRAILING VORTICES*

Alan J. Bilanin, Milton E. Teske,
Coleman duP. Donaldson and Richard S. Snedeker
Aeronautical Research Associates of Princeton, Inc.

SUMMARY

The mechanism of merging of like-signed aircraft vortices leads to a rapid redistribution of trailed vorticity in a wake through both convective and turbulent processes. Merging is investigated experimentally in a small wind tunnel and analytically through the use of a code which computes turbulent transport using a second-order closure turbulent model. Computations are reported which demonstrate the merging phenomenon, and comparisons are made with experimental results. The usefulness of point vortex computations in predicting merging is explored. Limited computations have shown that jet exhaust does not appreciably alter the merging phenomenon. The effect of ambient atmospheric turbulence on the aging of an aircraft wake is investigated at constant turbulent dissipation rate. It is shown that under stable atmospheric conditions, when atmospheric macroscales are less than or equal to the vortex spacing, misleading results may be obtained. This conclusion cautions against using one parameter to characterize the ability of the atmosphere to dissipate aircraft wake vortices.

*The work reported here has been sponsored by NASA under Contract No. NAS1-13932 and by the AFOSR under Contract No. F44620-75-C-0051. The authors would like to thank Mr. G. G. Williamson for help with the computations and acknowledge numerous conversations on turbulent transport with their colleague, Dr. W. S. Lewellen.

I. INTRODUCTION

The hazard associated with an aircraft's trailing vortex wake is generally acknowledged to be the large rolling moments induced on an encountering aircraft. These rolling moments are related to the angular momentum contained in the wake itself. The magnitude of angular momentum can be directly estimated from the Betz roll-up model (ref. 1), which has received widespread use in recent years (refs. 2-5). The Betz roll-up technique specifies how the torque exerted by the lift distribution on a wing (see fig. 1) results in a distribution of angular momentum in the trailed vortex through the relationships

$$r = \bar{y}(y) - Y \tag{1}$$

$$\Gamma(r) = \Gamma(y) \tag{2}$$

where $\Gamma(y)$ is the circulation distribution on the wing and $\Gamma(r)$ is the circulation distribution in the downstream vortex. The length r is related to y through Eq. (1), where $\bar{y}(y)$ is the centroid of vorticity shed outboard of wing station y and is defined as

$$\bar{y}(y) = \frac{-1}{\Gamma(y)} \int_y^s \frac{d\Gamma(\eta)}{d\eta}\, \eta\, d\eta \tag{3}$$

Equations (1) through (3) are equivalent to

$$\text{Torque} = \int_Y^s \ell(\eta)[\eta - \bar{y}(y)]d\eta = 2\pi\rho_o \int_0^r U_\infty V_\theta(\chi)\chi^2 d\chi \tag{4}$$

where $\ell(\eta) = -\rho_o U_\infty \Gamma(\eta)$ is the wing sectional loading on the fluid and s is the wing semispan.

The axial flux of angular momentum in a vortex of radius r equals the torque exerted on the fluid (calculated about $\bar{y}(y)$ outboard of wing station y). Setting $y = 0$ in Eq. (4) shows that the torque exerted by the wing equals the axial flux of angular momentum in the Betz vortex and is given by

$$\text{Torque} = \frac{Lb}{4}\left[\frac{\bar{y}(0) - \bar{y}_L}{s}\right] \tag{5}$$

where $\bar{y}_L$ is the centroid of the load distribution defined by

$$\bar{y}_L = \frac{\int_0^s \Gamma(\eta)\eta \, d\eta}{\int_0^s \Gamma(\eta) \, d\eta} \tag{6}$$

Since $(\bar{y}(0) - \bar{y}_L)/s$ is a function only of the shape of the load distribution, its value is nearly constant among various aircraft. (For a rectangularly loaded wing and a linearly loaded wing $(\bar{y}(0) - \bar{y}_L)/s = 1/2$ and $1/6$, respectively.) It is therefore not surprising that the rolling moment hazard is a function of the generating aircraft's size, since the angular momentum in the Betz vortex (from eq. (5)) is proportional to the product of the lift L and wing span b. If a small aircraft were to encounter the whole of this torque from a jumbo jet, the results would be disastrous.

Fortunately, the torque induced on an encountering aircraft is a fraction of that which might actually be extracted from the wake. This is due simply to the fact that the encountering aircraft's dimensions permit it to span only a portion of the vortex at any one time. This may not however be a saving grace, since the roll control capability of an aircraft diminishes with diminishing span. What then will permit a small aircraft to fly at a reasonable distance behind a larger generating aircraft? The answer lies in the distribution of angular momentum. First, the conservation of angular momentum would say that the total axial flux of angular momentum in the half-cross plane calculated about the aircraft wing centerline must initially equal the generator's wing root bending moment. Apparently the distribution of angular momentum can be substantially altered by tailoring the generator's lift distribution. Second, the landing or takeoff wake of an aircraft, comprised of multiple vortex pairs (see fig. 2), can undergo an

initially convective instability called vortex merging. The merging phenomenon results in a redistribution of trailed vorticity in a wake through convective and turbulent processes. This redistribution lessens the hazard of the trailed wake in distances which have been observed to be tens of spans behind the generating aircraft.

The convective and turbulent interactions between vortices in distances of up to 30 or 40 spans behind the generator form the subject of this paper. A qualitative description of the aging process in the near vortex wake and the relevance of multiple vortices and merging are discussed in Section 11. In Section III, A.R.A.P.'s turbulent model is briefly reviewed, and a simple merging computation between two equal strength like-signed vortices is given. Recent experimental results of the vortex-vortex interaction problem obtained in a small wind tunnel are described in Section IV. A discussion of how point vortex computations can be used to determine whether strong vortex interactions are likely to occur in vortex wakes is given in Section V. Numerical calculations of aircraft wakes including the effects of thrust and atmospheric turbulence are presented in Section VI. Finally, in Section VII, conclusions are offered.

SYMBOLS

A	wing aspect ratio .
b	wing span
b'	separation between two oppositely signed vortices
C_D	drag coefficient
C_L	lift coefficient
C_T	thrust coefficient
d	separation between like-signed vortices
e	circulation box size
h	vertical height of vortex pair
ℓ	sectional lift on the fluid
L	lift

P	pressure
q	$\sqrt{\overline{uu} + \overline{vv} + \overline{ww}}$
r	radial coordinate
r_c	viscous core radius
s	wing semispan
s'	$b'/2$
t	time
U,V,W	velocity components in the x,y,z Cartesian system
U_∞	flight speed
V_θ	swirling velocity
x,y,z	Cartesian coordinate system
$\bar{y}(y)$	centroid of trailed vorticity
$\bar{y}_L$	centroid of the load distribution
Γ	circulation
Γ_o	wing root circulation
ζ	vorticity
ε	turbulent dissipation rate
Λ	turbulent macroscale or integral scale parameter
ν	kinematic viscosity
ρ_o	ambient density
ψ	secondary streamline value
$\overline{\quad}$	overbar denotes time average

II. A QUALITATIVE DESCRIPTION OF VORTEX WAKE AGING

When an aircraft in a clean (cruise) configuration trails a wake, two regions of somewhat concentrated vorticity are left in the fluid, shown schematically in figure 3. For an encountering aircraft whose span is less than the semispan of the generating aircraft, a most desirable piece of information is the intensity of the swirling flow in a circular area whose diameter is the wingspan of the encountering aircraft. If circulation is a

reasonable measure of this intensity, then we must determine how circulation might decrease in this region, If we center the area about the centroid of shed vorticity (as in fig. 3), we see that vorticity cannot be transported from this region by convection since, roughly speaking, streamlines do not leave the circular region. Hence, diffusion is the only mechanism able to spread vorticity and reduce circulation in this area. Unfortunately, the axisymmetric vortex is quite stable and can only sustain low turbulence levels. In fact, turbulence is actually damped in the central region of the vortex (the viscous core). It is just in this region where vorticity is maximum, making it desirable to distribute this vorticity rather extensively over the wake half-plane. Apparently, however, only molecular transport provides any diffusion of vorticity here.

That vortex cores from simply loaded wings are in fact nearly laminar can be seen from figure 4 where smoke released from a tower has been entrained into the wing tip vortex of a large aircraft. The air through which the aircraft flies is discernibly turbulent (as interpreted from the dispersion of smoke) while the vortical fluid making up the viscous core is nearly laminar.

Turbulent computations using second-order closure modeling also confirm this feature of isolated vortices. The swirling velocity for a classical Lamb vortex is given by

$$V_\theta = \frac{\Gamma}{2\pi r}\left(1 - \exp\frac{r^2}{r_c^2}\right) \qquad (7)$$

Taking the equilibrium, nondiffusive, and high Reynolds number limits of the second-order closure model (ref. 6), we obtain the turbulent kinetic energy distribution shown in figure 5. Also shown is the corresponding distribution of vorticity. Note that no turbulent kinetic energy is predicted for $r/r_c \leq 1.25$. The centrifugal effect of the swirling velocity suppresses the Production of turbulence in this region.

From observations and analytic considerations (refs. 5,7), aircraft vortices do not produce sufficient axial shear to provide a mechanism for any sizable production of turbulence. The vortices from a clean aircraft age quite independently in a calm atmosphere. (The vortex pair from a clean aircraft can undergo a Crow instability excited by the atmosphere (ref. 8). However, time scales for this instability result in distances behind the aircraft far larger than those being considered here.)

In the landing or take-off configuration (flaps deployed), the trailed wake takes on a decidedly more complex structure. Multiple vortex pairs are trailed and interact. Significantly, this interaction may be favorable since the straining effect of vortex upon vortex may destroy the circular symmetry of each vortex. The vortices undergo an initial convective instability leading to a production of turbulent energy and turbulent redistribution of the vorticity (again, see fig. 3). On comparable time scales, the multiple-pair wake can age more than the wake of the cruise aircraft when this favorable interaction is utilized.

Of course, other mechanisms can also act to spread vorticity across the wake. However, only vortex breakdown acts on a time scale commensurate with the merging phenomenon. Unfortunately, our work on the transport processes involved in breakdown is just beginning.

In sum, the merging phenomenon is a naturally occurring mechanism of decay in aircraft multiple-vortex wakes, leading to a more rapid conversion of the kinetic energy of the swirling velocities in the vortices into turbulent kinetic energy. If the merging phenomenon can be understood and predicted, a great potential exists for lessening the hazard associated with vortex wakes through suitably tailored wing lift and drag distributions.

III. A NUMERICAL COMPUTATION OF MERGING

Dunham (ref. 9) first observed the merging phenomenon between flap and tip vortices of the B-747 aircraft on what has become the LDG/O configuration. That is, inboard flaps are deployed at $\delta_f = 46^\circ$ and midspan flaps remain undeployed. His sketch of the phenomenon is shown in figure 6, where ink injected at the wing was used to visualize the vortices. He observed that the tip and flap vortices, while quite distinct at fifteen span-lengths behind the B-747, appeared to interact further downstream until only one rather weak (diffuse) vortex remained. The rather rapid diffusion of the ink suggested the mechanism of turbulent transport in the spreading of the trailed vorticity.

To model the convection and turbulent diffusion of vorticity, we at A.R.A.P. have developed a computer code to solve the equations of fluid motion including our invariant turbulent model (ref. 10). This model is based on a closure of the rate equations for the velocity correlations at the second order. Details of the model, its evolution and validation, may be found in references 10 and 11. It suffices here to reproduce the equations. The flow variables are separated into mean and fluctuating components, then averaged and modeled where appropriate. The mean variables satisfy continuity

$$\frac{\partial U_i}{\partial x_i} = 0 \tag{8}$$

and momentum

$$\frac{\partial U_i}{\partial t} + U_j \frac{\partial U_i}{\partial x_j} = - \frac{\partial \overline{u_i u_j}}{\partial x_j} + \nu \frac{\partial^2 U_i}{\partial x_j^2} - \frac{1}{\rho_o} \frac{\partial P}{\partial x_i} \tag{9}$$

where the density ρ_o is constant.

The turbulent velocity correlations satisfy the rate equations

$$\frac{\partial \overline{u_i u_j}}{\partial t} + U_k \frac{\partial \overline{u_i u_j}}{\partial x_k} = \underbrace{- \overline{u_i u_k} \frac{\partial U_j}{\partial x_k} - \overline{u_j u_k} \frac{\partial U_i}{\partial x_k}}_{\text{Production}} \tag{10}$$

$$+ v_c \underbrace{\frac{\partial}{\partial x_k} \left(q \Lambda \frac{\partial \overline{u_i u_j}}{\partial x_k} \right)}_{\text{pressure and velocity diffusion}}$$

$$- \frac{q}{A} \underbrace{\left(\overline{u_i u_j} - \delta_{ij} \frac{q^2}{3} \right)}_{\text{tendency toward isotropy}}$$

$$+ \nu \underbrace{\frac{\partial^2 \overline{u_i u_j}}{\partial x_k^2}}_{\text{viscous diffusion}}$$

$$- \delta_{ij} \underbrace{\frac{2bq^3}{A} - \frac{2a\nu \overline{u_i u_j}}{\Lambda^2}}_{\text{dissipation}}$$

where $q = (\overline{u_i u_i})^{1/2}$. The pressure and velocity diffusion, tendency toward isotropy, and dissipation terms are modeled. Models are chosen on the basis of dimensional consistency, tensor invariancy under transformation, and physical considerations (ref. 11). The constants v_c, b, and a have the values 0.3, 0.125, and 2.5, respectively. These constants have been determined from appropriate experiments so chosen where possible to emphasize the particular effect studied.

Lambda (A) is the turbulent integral scale or macroscale parameter gaging the coherent length scale of the turbulent eddies. It is determined from a dynamic equation which models the production, diffusion, and dissipation of the integral scale'of the turbulence. The dynamic scale equation being used (ref. 11) is

$$\frac{D\Lambda}{Dt} = \underbrace{0.35\,\frac{\Lambda}{q^2}\,\overline{u_i u_j}\,\frac{\partial U_i}{\partial x_j}}_{\text{production}} + \underbrace{0.6\,\frac{\nu}{\lambda^2}\,A}_{\text{dissipation}} + \underbrace{0.3\,\frac{\partial}{\partial x_i}\left(q\Lambda\,\frac{\partial \Lambda}{\partial x_i}\right) - \frac{0.375}{q}\left(\frac{\partial q\Lambda}{\partial x_i}\right)^2}_{\text{diffusion}} \tag{11}$$

where $\lambda = \dfrac{A}{[a+(bq\Lambda/\nu)]^{1/2}}$ is the dissipation scale.

Equations (8-11) have been programmed to solve either two-dimensional unsteady or three-dimensional steady problems with a parabolic approximation made in one space dimension. The details of the algorithms used can be found in reference 12.

As a first illustration of the numerical computations, we have chosen the simplest merging problem between two like-signed equal strength vortices. The computational region is shown in figure 7. Two Gaussian spots of vorticity of the form

$$\frac{\pi d^2 \zeta}{2\Gamma} = \frac{d^2}{2r_c^2}\exp\left(-\frac{r^2}{r_c^2}\right) \tag{12}$$

have been placed at $y = \pm d/2$, $z = 0$. The radius r is measured outward from both $y = \pm d/2$, $z = 0$. Gaussians of turbulent kinetic energy of the form

$$q^2 = q_o^2 \exp\left(-\frac{r^2}{r_c^2}\right) \tag{13}$$

are also placed at $y = \pm d/2$, $z = 0$ with

$$q_0^2 = 0.01\left(\Gamma/\pi d\right)^2 \tag{14}$$

The calculation is started with $\overline{uu} = \overline{vv} = \overline{ww} = q^2/3$ and $\overline{uv} = 0$. The integral scale parameter is initially taken equal to 0.2s. Boundary conditions on velocity are applied via a multipole expansion of the vorticity field (ref. 12). Turbulent quantities are set equal to zero at the computational boundaries.

The results of the computations are shown in figures 8, 9, and 10, where instantaneous distributions of pressure, vorticity, and turbulent kinetic energy are shown in intensity form. The counter-clockwise rotation of the pair is expected. It is interesting to note that the mean flow variables, pressure and vorticity, take on a discernibly more axisymmetric structure at $t\Gamma/\pi d^2 = 4$ than the turbulent kinetic energy, This is expected in a phenomenon in which the redistribution of vorticity is initially governed by convection. The initial time scale for turbulent redistribution through diffusion is of the $O(\Lambda/q)$, which is approximately $t\Gamma/\pi d^2 = 1$.

A comparison with an equivalent isolated vortex decay computation illustrates the significance of the merging phenomenon in terms of aging the vortex flow field. We have chosen to compute the decay of an isolated axisymmetric vortex whose initial vorticity distribution is Gaussian and whose circulation equals that of the pair. The core radius r_c has been chosen to make the polar moment of the vorticity distribution computed about the centroid equal to that of the merging pair. Thus,

$$r_c^2 = r_{c_{pair}}^2 + \frac{d^2}{4} \tag{15}$$

The computation is carried out with an axisymmetric version of the code (ref. 13) used to compute the merging of the like-signed pair. The initial turbulence distribution is taken to be $\overline{uu} = \overline{vv} = \overline{ww} = q^2/3$ where

$$q^2 = 2.0q_o^2 \exp\left[-\left(\frac{r}{r_{c_{pair}}}\right)^2\right] \qquad (16)$$

so that the initial total turbulent kinetic energy in both computations are equal. The integral scale parameter A is taken to be 0.2s ,

Figure 11 shows the total turbulent kinetic energy in the crossplane as a function of time. The level that can be supported by the axisymmetric isolated vortex is far less than initially introduced, as discussed earlier and in reference 6. However, the breakdown of the axisymmetric structure about each vortex in the merging pair results in the production of turbulent kinetic energy and, hence, Reynolds stresses, which diffuse the mean vorticity outward in addition to the convective spreading. The production of turbulence is the transport mechanism which can diffuse vorticity to the wake centerline and result in the decay of circulation in the wake, as was shown schematically in figure 3.

IV. EXPERIMENTAL OBSERVATIONS OF MERGING AND PAIR INTERACTIONS

A simple experiment was designed to observe the merging phenomenon in a controlled environment.

Apparatus and technique

Flow visualization studies of vortex merging and pairing were carried out in A.R.A.P.'s 0.305 m × 0.305 m subsonic wind tunnel. This facility has a 2-m-long test section with an adjustable roof to allow modification of the axial pressure gradient. For these studies the pressure gradient was set at zero.

The tunnel has a maximum velocity capability of 15 m/sec and the test section turbulence level is relatively low -- about 0.2% For the purposes of these studies, the test section was fitted with windows for its full length on one side, and the interior

surfaces were painted flat black to improve visibility of the white smoke used for visualization.

Vortex flows were produced by airfoils mounted through opposite sidewalls of the tunnel just upstream of the test section. Each airfoil had a constant chord of 7.62 cm and was mounted so that its angle of attack and length of immersion in the stream could be adjusted. Thus, the strengths of the vortices and their initial spacing could be set to any desired value. The airfoil section was NACA 0012 and the tip was a revolved section. Construction was of molded fiber glass and polyester resin. The airfoils were hollow to permit the flow of smoke from outside the tunnel to holes in the wing tips near the points of initial vortex roll-up. This arrangement produced a quite satisfactory concentration of smoke in the trailed vortex behind each airfoil.

Observation of merging and pairing phenomena was accomplished by illuminating the entrained smoke with a planar beam of light directed across the tunnel normal to the flow. In this way a cross-section of the vortex flow pattern was made visible when viewed from a point upstream or downstream of the light beam. In order to record the patterns photographically, a small mirror was mounted inside the wall of the diffusor downstream of the test section. The mirror was set so as to reflect an image of the illuminated cross-section through a window in the side wall and, finally, to a camera outside the tunnel. With this setup it was possible to photograph patterns between 3 and 23 chord-lengths downstream of the airfoils.

Continuous illumination was provided by the beam from a lantern slide projector and instantaneous illumination was provided by an electronic flash unit. Thus, it was possible to view smoke patterns that were either time averaged (usually 1/2-second exposure) or "frozen" (1/2800 second). The planar beam of desired intensity was produced by passing the light through a vertical slit about 0.95 cm wide.

A sufficient quantity of dense white smoke was produced by a boiled-kerosene smoke generator.

Views of the wind tunnel and airfoil assemblies are shown in figure 12.

Results

The merging phenomenon between vortices of same sign and strength is visualized in figure 13. Viewed from downstream, the angles of attack for the left and right wings are -6° and 6°, respectively. The vortex rotation is then in the clockwise direction. As can be seen, the vortices are quite distinct at $x/d = 18$ but merge quite rapidly between $x/d = 90$ and 114. By $x/d = 138$, the merged pair is nearing an axisymmetric shape. The straining effect of vortex upon vortex is quite evident at the $x/d = 114$ and 126 stations.

The photographs suggest that the merging phenomenon is nearly laminar. This is attributed to rather low test Reynolds numbers. Typically, $\Gamma/\nu \simeq 5000$ for these tests, while the Reynolds numbers associated with aircraft wakes are more like 10^7. This, however, does not limit the usefulness of these tests since the initial stages of the merging phenomenon are convection dominated. The initial redistribution of trailed vorticity can be studied directly.

To again illustrate the importance of turbulent transport, the merging computation presented in Section III is compared with smoke visualization photographs. Figure 14 shows computed vorticity intensity plots and photographs of visualized smoke at comparable downstream positions. The comparison of smoke intensity with vorticity is not quite correct since the smoke particles are not quite the same density as the fluid. The comparisons, however, are qualitatively quite good with the last axial station showing the greatest departure. The turbulent computation shows the vorticity measurably more spread through the fluid and at a substantially lower level. Both effects result from the turbulent diffusion present in the numerical simulation.

The next sequence of photographs, shown in figure 15, explores angle-of-attack change of one wing while holding vortex separation and the angle of attack of the second wing constant. The photographs are taken at downstream station $x/d = 55.4$. Equal sign and strength vortices occur with $\alpha_{ref} - - \alpha_{var} = - 6^{\circ}$. As one vortex is weakened, the stronger vortex begins to strain the weaker vortex and proceeds to wrap the weaker vorticity around itself. When the vortices become of' opposite sign, there is less tendency to merge even when one vortex is significantly weaker than the other. Compare, for instance, $\alpha_{ref} = - 6^{\circ}$, $\alpha_{var} = 2^{\circ}$, and $a_{ref} = - 6^{\circ}$, $a_{var} = - 2^{\circ}$. When both angles of attack are equal the classical vortex pair is produced.

The next sequence of photographs (fig. 16) explores the stability of the counter-rotating pair as the separation between the pair is reduced. At a fixed downstream station, the vortex pair has descended to a lower position in the tunnel as separation is decreased. The last photograph shows how remarkably stable the counter-rotating configuration can be. The physical mechanisms which permit vortices of like sign to merge quite readily while inhibiting the merging of vortices of opposite sign are yet to be explained, Moore and Saffman's work (ref. 14) notwithstanding.

In figure 17 an attempt is made to visualize the structure of the vortex by taking a high-speed photograph (1/2800 sec). Upper right shows the instantaneous smoke pattern of an unmerged pair, while upper left shows the continuously lighted smoke distribution, Lower right shows the instantaneous smoke pattern of a merging pair with equal strength and like sign. This may be compared to the continuously lighted photograph in lower left. A careful inspection of the instantaneously lighted photographs shows the merged pair to be more turbulent than the unmerged pair.

V. MERGING COMPUTATIONS USING POINT VORTICES

An important part of the merging phenomenon is the production of turbulence and the subsequent diffusion of trailed vorticity. Before using a program that incorporates all of these effects, we may first obtain some fundamental results using a far simpler inviscid model, namely, the point vortex technique for computing wake structure. Point vortex computation for wakes is not a new idea, having been used first by Westwater (ref. 15) in 1935. Since that time, many investigators have used this technique. The basic idea is to distribute point vortices ip the Treffetz plane of a hypothetical wing, as shown in figure 18, and compute their trajectories in time. The resulting motion will be produced by the convective interaction between the vortices themselves.

Given two like-signed vortices, the rate of merging should increase as the separation between the vortices decreases. The simplest interesting wake is made of two vortex pairs; for example, one comprised of flap and tip vortices.

Merging should occur if the subsequently computed trajectories brought the flap and tip vortices closer together, or at least did not increase the distance between vortex centers. Figures 19 and 20 illustrate the trajectories of two rather differently structured wakes. The tight orbiting of flap and tip vortices in figure 19 will result in merging while the weak interaction between flap and tip vortices, shown in figure 20, may not result in merging.

For two-vortex-pair wakes a qualitative prediction of whether merging may in fact occur can be obtained from a wake classification chart shown in figure 21. When vortices are of like sign and fall in the region marked "remain together," one might expect that merging will eventually occur. On the other hand, wakes which fall in the region denoted "separate" may possibly remain unmerged. Wakes from real aircraft in a landing or takeoff configuration have far more structure than can be

represented simply by two vortex pairs. In fact, the B-747 aircraft in a landing configuration trails six discrete pairs if the tail vortex is included (ref. 6).

At the next level of complexity we consider a third vortex pair which can be used to model a fuselage vortex. We choose as a representative case the wake from the Landing/O configuration studied by NASA. The load distribution shown in figure 22 has been taken from the work of Ciffone and Lonzo (ref. 16). The Betz roll-up recipe will predict roll-up into three discrete vortices (ref. 2). The trajectories as viewed in the Treffetz plane are shown in figure 23. As can be seen, the distance between the flap and tip vortices continuously increases downstream. Ciffone and Lonzo conducted flow visualization experiments in a towing tank on this configuration and reported that merging did not occur. It is instructive to compute the separation between tip and flap vortices as a function of downstream distance while varying the strength of the fuselage vortex (fig. 24). By weakening the fuselage vortex, it is possible to reduce the separation between flap and tip vortices. The minimum separation between flap and tip vortices occurs when $\Gamma_j \simeq -0.3\Gamma_f$. Further reduction in fuselage vortex strength serves only to again increase the distance between flap and tip vortices.

In figure 25 the sensitivity of distance between flap and tip vortices is investigated as a function of the position of the fuselage vortex. By moving the fuselage vortex from $\bar{y}_j/s = 0.125$ to 0.2 (a shift of 7.5% of the semispan), the flap and tip vortices can be brought to a distance of only 9% of the wing semispan. The dots lying near the curve denoted $\bar{y}_j/s = 0$ correspond to the distance between flap and tip vortices in a fully two-dimensional unsteady solution of the equations of motion with the computer code described in Section 111. This computation is not described in this paper, but may be found in reference 12. It is heartening to see the good agreement between the transportative model and the simple point vortex calculation.

The above computations serve to demonstrate the sensitivity of wake geometry to modest changes in wing load distribution. It is an unfortunate fact that technologies to give accurate predictions of load distributions are somewhat lacking, particularly for wings with flaps and slats deployed. The magnitude of the loss of lift at the wing-fuselage junction quite strongly influences wake geometry. In our opinion, there is now a need to know the wing load distribution more accurately than ever before.

The next level of sophistication of computing roll-up and vortex-vortex interaction discretizes the shed. vorticity with a large number of point vortices. Various investigators have questioned the validity of such a model, particularly when computations proceed for any length of time. These criticisms have been reviewed in reference 6. However, if one is careful with numerics and physical interpretation of the results, it appears that a great deal can be learned from such a computation.

Figure 26 shows the modified Landing/O configuration at $C_L \cong 0.8$. This load distribution was represented by forty discrete vortices of equal strength. The subsequent positions are shown in figure 27. Plotted also are the positions of the flap, tip and fuselage vortices as obtained from a three-vortex-pair representation. These clusters are in reasonable agreement with the three-vortex-pair computations.

For a second computation we remove the fuselage vortex from the modified Landing/O configuration as shown by the dashed line on figure 26, still using forty equal strength vortices to represent the trailed vorticity. In figure 28 a comparison of the many vortices representation is made with a two-vortex-pair model. The results are quite acceptable.

Figure 29 shows the distance between the flap and tip vortex centroids, as computed above, with quite good agreement.

The study shown in figure 25 indicates that moving the fuselage vortex to 20% of the semispan of the wing causes the flap

and tip vortices to move into close proximity. The load distribution for the LDG/O configuration (fig. 22) was altered inboard to create a fuselage vortex of strength $\Gamma_j = -0.47\Gamma_f$. As it turned out, the fuselage vortex centroid was located at $\bar{y}/s = 0.185$. The separation between tip and flap vortices as a function of downstream distance is shown in figure 30. For this configuration, minimum separation of $d/s \cong 0.175$ is reasonably well predicted. However, the distances downstream at which this minimum is achieved do not compare favorably. When the fuselage vortex is removed, so that flap and tip vortices move apart, the computation using a distribution of vortices again compares favorably with computations using one point vortex to represent each discrete vortex in the wake. The discrepancy when distributions move together lies in the incorrect approximation that the centroid of a given distribution of vorticity moves at the velocity induced at its centroid by other concentrations. In reference 6 we show that the velocity of the centroid of a bounded region of vorticity in an infinite fluid is given by

$$\frac{d\vec{r}}{dt} = \frac{\int \vec{U}_o \zeta dA}{\Gamma} \qquad (17)$$

where $\vec{U}_o$ is the velocity field induced by the presence of all other concentrations of vorticity in the fluid other than the one whose motion is being computed. As two distributions come close together, $\vec{U}_o$ may vary significantly over ζ and the motion of the centroid is not simply the fluid velocity at the centroid induced by all other concentrations of vorticity.

Another significant result from this computation is that the calculation which used a distribution of point vortices did not show any tendency to merge. We add without further comment that the negative fuselage vortex was also in close proximity to the flap and tip vortices during closest approach.

It has been our purpose in this section to point out that simple discrete vortex computations can be used to quickly assess

whether particular lift distributions will result in a multiple vortex wake which will merge. When vortices of like sign remain in proximity of each other, the merging process must eventually occur. An estimation of the deintensification as a result of merging requires the use of a transportative fluid model, such as that presented in Section III. In sum, inviscid computations indicate that small changes in aircraft configuration and, hence, wing lift distribution can have a profound effect on wake structure. More accurate knowledge of lift distributions on commercial jet-liners, particularly in the landing and take-off configurations with and without landing gear deployed, would greatly aid in understanding the dynamics of aircraft vortex wakes.

VI. CALCULATIONS OF AGING IN AIRCRAFT VORTEX WAKES

Computations using the vortex wake code discussed in Section III are presented here to illustrate merging and the significance of engine exhaust and ambient atmospheric turbulence.

Decay of a simple vortex pair

Figure 31 shows the initial conditions of the computation of the decay of a simple vortex pair. The initial vorticity and turbulent kinetic energy distributions were taken to be Gaussian about $y/s' = \pm 1$. Two computations were made with the viscous core radius $r_c/s' = 0.4$ and 0.8. The integral scale parameter Λ/s' was taken equal to 0.2. The turbulent energy components were again equally distributed with $\overline{uu} = \overline{vv} = \overline{ww} = q^2/3$. The cross-correlations were initially taken to be zero.

The computations are carried out in time and the results transformed to downstream distance through $x = U_\infty t$. Figure 32 shows the circulation computed over the area $y \geq 0$. The constant circulation region for the initially tight vortex ($r_c/s' = .4$) illustrates the situation depicted in figure 3. Circulation cannot decrease until the vorticity has diffused across the wake.

The computation for the initially more diffuse vortex ($r_c/s' = .8$) has been carried downstream to a distance of $x'/b' = 8\pi Ab'^2/b^2C_L$; at $C_L = 1$ and $A = 7$ and a rectangularly loaded wing, $x/b \simeq 160$. For a B-747 aircraft this is approximately 10 km. Without ambient atmospheric turbulence, the vortex pair ages quite slowly. Figure 33 compares the maximum root-mean-square turbulence level q between the pair and a computation using a single isolated vortex having the same initial conditions as one vortex of the pair. The level of turbulent intensity in the pair is not significantly different than that computed for an isolated vortex,

In figure 34 we show the $r_c/s' = 0.8$ circulation as a function of downstream distance about a square of side 2e, centered at the centroid of vorticity in the half-plane. As might be expected, the decay of circulation is far more rapid than the half-plane value.

Figure 35 shows the computed descent rate dh/dt of the vertical centroid $\bar{z}$ of the vorticity. The $\bar{z}$ increases as a function of downstream distance since a uniform upwash has been added to the cornputation (of magnitude $\Gamma_o/4\pi s'$) to keep the vortex pair centered in the computational mesh. The descent rate decreases as vorticity diffuses across the aircraft centerline.

In figures 36 and 37 are shown instantaneous streamlines at the beginning and end of the computation for the $r_c/s' = 0.8$ computation. The y,Z coordinate system is one in which the fluid at infinity is at rest; therefore, the pair descends downward.

Merging of equal strength flap and tip vortices, including engine exhaust

Vortices are positioned at $y/s = -.95$, $-.4$, $.4$ and $.95$, and $z/s = 0$. In the right-half plane the vortices are of equal strength and of positive sign. In the left-half plane the vortices are of equal strength and negative sign. The vorticity distributions are given by Gaussians

$$\frac{\zeta 2\pi s^2}{\Gamma} = \frac{2s^2}{r_c^2} \exp\left(-\frac{r^2}{r_c^2}\right) \tag{18}$$

and the turbulent kinetic energy distribution about each vortex is given by

$$\left(\frac{2\pi sq}{\Gamma}\right)^2 = 0.01 \quad p\left(-\frac{r^2}{r_c^2}\right) \tag{19}$$

with the turbulent energy components again equally divided initially. Cross correlations are initially taken to be zero.

A second computation uses the above initial conditions but adds the jet exhaust. At a lift coefficient of 1.5 and assuming $C_D = C_T = 0.125C_L$, the axial velocity excess about each engine is given by

$$\frac{\Delta U 2\pi s}{\Gamma} = 8.0 \exp\left(-52.0\ \frac{r^2}{s^2}\right) \tag{20}$$

Taking the aspect ratio equal to 7, the flight speed is $40.0\Gamma/2\pi s$. The engine exhausts are Gaussians of excess axial velocity and are positioned at $y/s = -0.75$, -0.4, 0.4, and 0.75 and $z/s = -0.08$. Except for a vertical displacement of $z/s = -0.08$, the inboard engines exhaust directly into the flap vortices. Additional Gaussian distributions of turbulent kinetic energy are positioned at each engine with the distribution given by

$$\left(\frac{2\pi sq}{\Gamma}\right)^2 = 0.64 \exp\left(-52.0\ \frac{r^2}{s^2}\right) \tag{21}$$

The turbulent energy components are equally partitioned and the cross correlations taken to be zero initially.

Figure 38 shows a comparison of the trailed vorticity in intensity plot form. The darkest areas have intensity equal to unity, since the plots have been made by nondimensionalizing the vorticity with the maximum value at $x/b = 0$. As can be seen, the jet engines do not hinder the merging of flap and tip vortices.

At twelve spans downstream the jet engines give slightly more spreading of the trailed vorticity; hence, the lower maximum value.

Figure 39 shows the intensity of the turbulent kinetic energy. Note that the normalization differs between the run with and without jet exhaust. It is likely that appreciable redistribution of the trailed vorticity is yet to occur owing to the large values of turbulent kinetic energy in the wake. This feature is overemphasized by taking the initial integral scale parameter Λ/s to be 0.2 for both runs. The integral scale parameter in the exhaust jets should be initialized to be somewhat smaller. In any case, the merging phenomenon is not significantly altered by jet exhaust and its accompanying turbulence.

Jet exhaust axial velocity excess intensity plots are shown in figure 40. Note that the inboard engine exhaust which was introduced into the flap vortex is slower to decay than the exhaust from the outboard engine, again demonstrating the suppression of the production of turbulence by swirl.

Wake dissipation by atmospheric turbulent diffusion of vorticity

There has been an attempt (ref. 8) to correlate wake lifetime with the turbulent dissipation rate ε (our model at high Reynolds number gives $\varepsilon = 0.125q^3/\Lambda$). Vortices present their greatest hazard under stable atmospheric conditions. Under these conditions, scales can be smaller than the characteristic wake length scale - the vortex spacing. Under these problem atmospheric conditions, the turbulent dissipation rate does not contain sufficient information to estimate the diffusion of trailed vorticity by the atmosphere. The integral- or macro-scale must be known. This fact can be demonstrated by two computations in which ε is held constant. For light and light-to-moderate turbulence, we use a value of $\varepsilon^{1/3} = 2\ cm^{2/3}/sec$ as suggested in reference 8.

If we take $\Lambda/s = 0.2$ and 2.0, the corresponding turbulent kinetic energies become $(2\pi sq/\Gamma)^2 = 0.025$ and 0.116, respectively. These two values can probably be achieved in a stable atmosphere with conventional jetliners.

The initial conditions are again Gaussians of vorticity at $y/s = \pm 1$ of opposite sign to produce a counter-rotating pair. The viscous core radius is taken to be $r_c/s = 0.5$. The turbulent energy components are again equally distributed so that $\overline{uu} = \overline{vv} = \overline{ww} = q^2/3$ initially. Integral scale parameter and turbulent energy components are held constant on the computational boundaries.

Figure 41 shows the circulation decay computed about a box contour of side 2e centered at the centroid of the vorticity. At the end of the computation (typically a wake age of 60 sec), levels differ by a factor of two. More importantly, the rate of decay differs by approximately a factor of four. These results do well to emphasize the importance of scale and caution against too simple a parameterization of the atmosphere. Obviously, the effects of wind shear and stratification help to make the analysis of the interaction of a vortex wake with the atmosphere a most difficult one.

An indirect comparison can be made between the above results and figure 34, which gives circulation decay of a vortex pair in a quiescent atmosphere. The initial spread of vorticity is different in that $r_c/s = 0.8$ for the pair in the quiescent atmosphere, while $r_c/s = 0.5$ for the above cases. The abscissa on figures 32 and 41 are equal and so time or downstream positions can be compared directly. The slow decay of the pair in a quiescent atmosphere is clearly demonstrated. The dominance of the atmosphere in controlling the ultimate death of a vortex wake is absolute even for low ambient turbulence levels. The turbulent atmosphere may be likened to an infinite reservoir of turbulent kinetic energy which can, for unlimited time, nibble away at the vortex wake.

Work is currently underway at A.R.A.P. to investigate through second-order closure turbulent modeling the fluid dynamics of the lower atmosphere. This work (partially reported in ref. 17) should give those of us concerned with the vortex hazard the tools necessary to access the rate of wake aging which results from interaction with a dynamic atmosphere.

VII. CONCLUSIONS AND RECOMMENDATIONS

The phenomenon of vortex merging has been investigated experimentally in a wind tunnel and numerically through the use of a computer code, which includes transport via a second-order closure turbulent model. It is shown that the merging phenomenon between like-signed vortices is a mechanism which results in redistribution of the trailed vorticity through convective and turbulent mechanisms. This redistribution is one which extensively spreads the vorticity over the wake and therefore hastens the decay process. Comparisons between experimental observations of vortex merging and numerical simulation of the phenomenon are favorable.

The usefulness of discrete point vortex computations to investigate wake geometry and structure is discussed, It is shown that small changes in the strength and/or initial position of the fuselage vortex can have a profound effect on the structure of the multiple-vortex-pair wake.

Using the transportative code, computations have been run which demonstrate merging between like-signed and strength flap and tip vortices with and without engine jet exhaust. The merging phenomenon does not appear to be significantly altered by the jet exhaust.

The effect of ambient atmospheric turbulence on the aging of an aircraft wake is investigated at constant turbulent dissipation rate. It is shown that under stable atmospheric conditions, when atmospheric macroscales may be less than or equal to the vortex

spacing, misleading results may be obtained if vortex aging is correlated only with the turbulent dissipation rate. This result cautions against using one parameter to characterize the ability of the atmosphere to dissipate aircraft wake vortices.

The technology now exists to investigate the complex convective and diffusive processes in aircraft vortex wakes. However, to use this technology requires an accurate description of the wing load distribution - a quantity not easily predicted for all but cruise-configured wings. It is recommended that accurate load distributions be obtained experimentally for the B-747 aircraft. These data will surely be of use in both understanding the interactions which result in a minimum hazard wake as well as permitting this technology to be transferred to other jumbo jetliners.

There is yet the problem of ground plane-vortex wake interaction. Hopefully, the merging phenomenon with its resulting transportative mechanisms will still be active.

REFERENCES

1. Betz, A.: Behavior of Vortex Systems. NACA TM 713 (trans. from ZAMM, Vol. XII.3, 1932).

2. Donaldson, C. duP., R.S. Snedeker, and R.D. Sullivan: A Method of Calculating Aircraft Wake Velocity Profiles and Comparison with Full-scale Experimental Measurements. J. Aircraft 11, 9, September 1974, pp. 547-555.

3. Rossow, V.: On the Inviscid Rolled-up Structure of Lift-Generated Vortices. J. Aircraft 10, 11, November 1973, pp. 647-650.

4. Jordan, P.: Structure of Betz Vortex Cores. J. Aircraft 10, 11, November 1973, pp. 691-693.

5. Bilanin, A.J., and C. duP. Donaldson: Estimation of Velocities and Roll-Up in Aircraft Vortex Wakes. J. Aircraft 12, 7, July 1975, pp. 578-585.

6. Donaldson, C. duP., and A.J. Bilanin: Vortex Wakes of Conventional Aircraft. AGARD-AG-204, May 1975.

7. Moore, D.W., and P.G. Saffman: Axial Flow in Laminar Trailing Vortices. Proceedings of the Royal Society: Ser. A: Mathematical and Physical Sciences' 333, 1973, pp. 491–508.

8. Tombach, I.: Observations of Atmospheric Effects of Vortex Wake Behavior. J. Aircraft 10, 11, November 1973, pp. 641–647.

9. Dunham, R.E., Jr.: Model Tests of Various Vortex Dissipation Techniques in a Water Towing Tank. NASA LWP-1146, January 1974.

10. Donaldson, C.duP.: Atmospheric Turbulence and the Dispersal of Atmospheric Pollutants. EPA-R4-73-016a, March 1973.

11. Lewellen, W.S., and M.E. Teske: Turbulence Modeling and its Application to Atmospheric Diffusion. Part 11: Critical Review of the Use of Invariant Modeling. EPA-600/4-75-016a, August 1975.

12. Bilanin, A.J., M.E. Teske, C. duP. Donaldson, and G.G. Williamson: Vortex Interactions and Decay in Aircraft Wakes. A.R.A.P. Report No. 271, May 1976.

13. Sullivan, R.D.: A Program to Compute the Behavior of a Three-Dimensional Turbulent Vortex. ARL-TR-74-0009, December 1973.

14. Moore, D.W., and P.G. Saffman: Structure of a Line Vortex in an Imposed Strain. Aircraft Wake Turbulence and its Detection (J.H. Olsen, A. Goldburg, M. Rogers, eds.), Plenum Press, New York, 1971, pp. 339–354.

15. Westwater, F.L.: Rolling Up of the Surface of Discontinuity Behind an Aerofoil of Finite Span. A.R.C. R&M 1962, 1935.

16. Ciffone, D.L., and C. Lonzo, Jr.: Flow Visualization of Vortex Interactions in Multiple Vortex Wakes Behind Aircraft. NASA TM X-62,459, June 1975.

17. Lewellen, W.S., and G.G. Williamson: Wind Shear and Turbulence Around Airports. A.R.A.P. Report No. 267, January 1976.

18. Bradshaw, P.: The Effects of Streamline Curvature on Turbulent Flow. AGARDograph 169, August 1973.

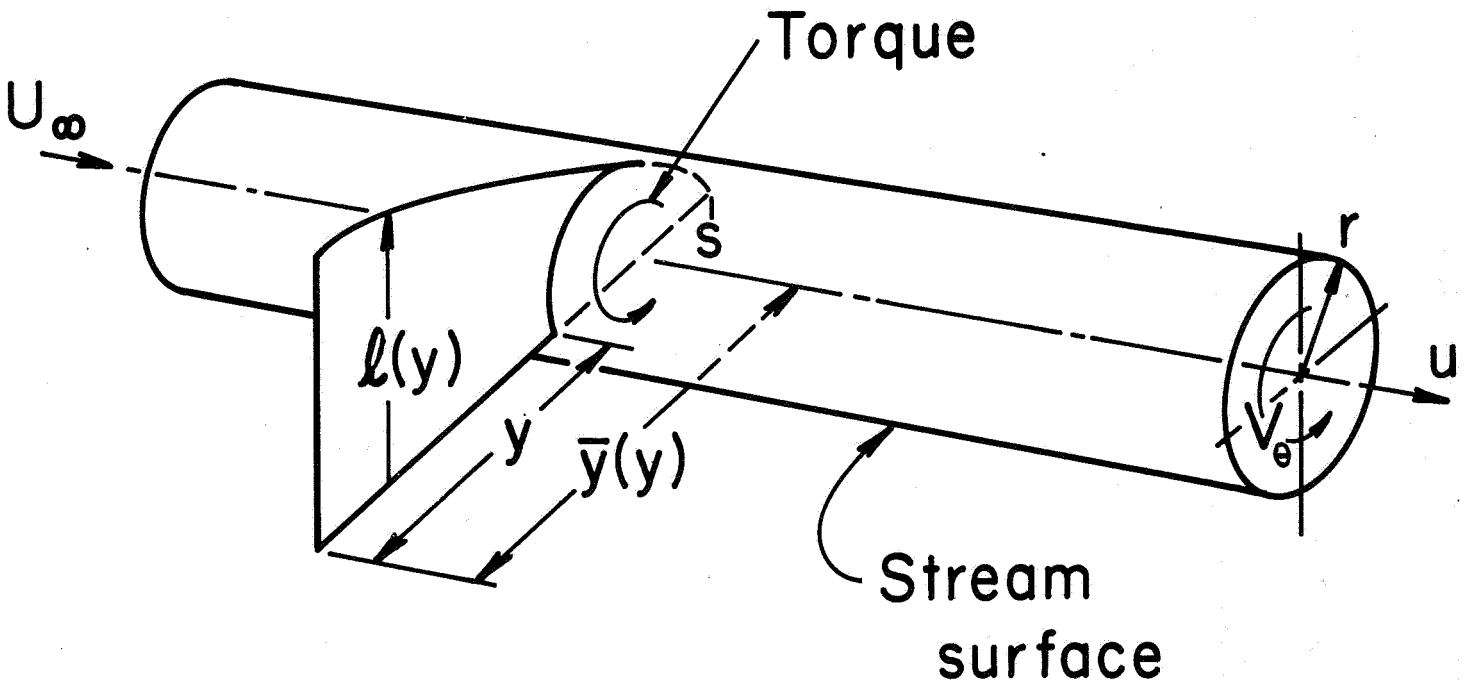

Figure 1. Geometry of the Betz roll-up model

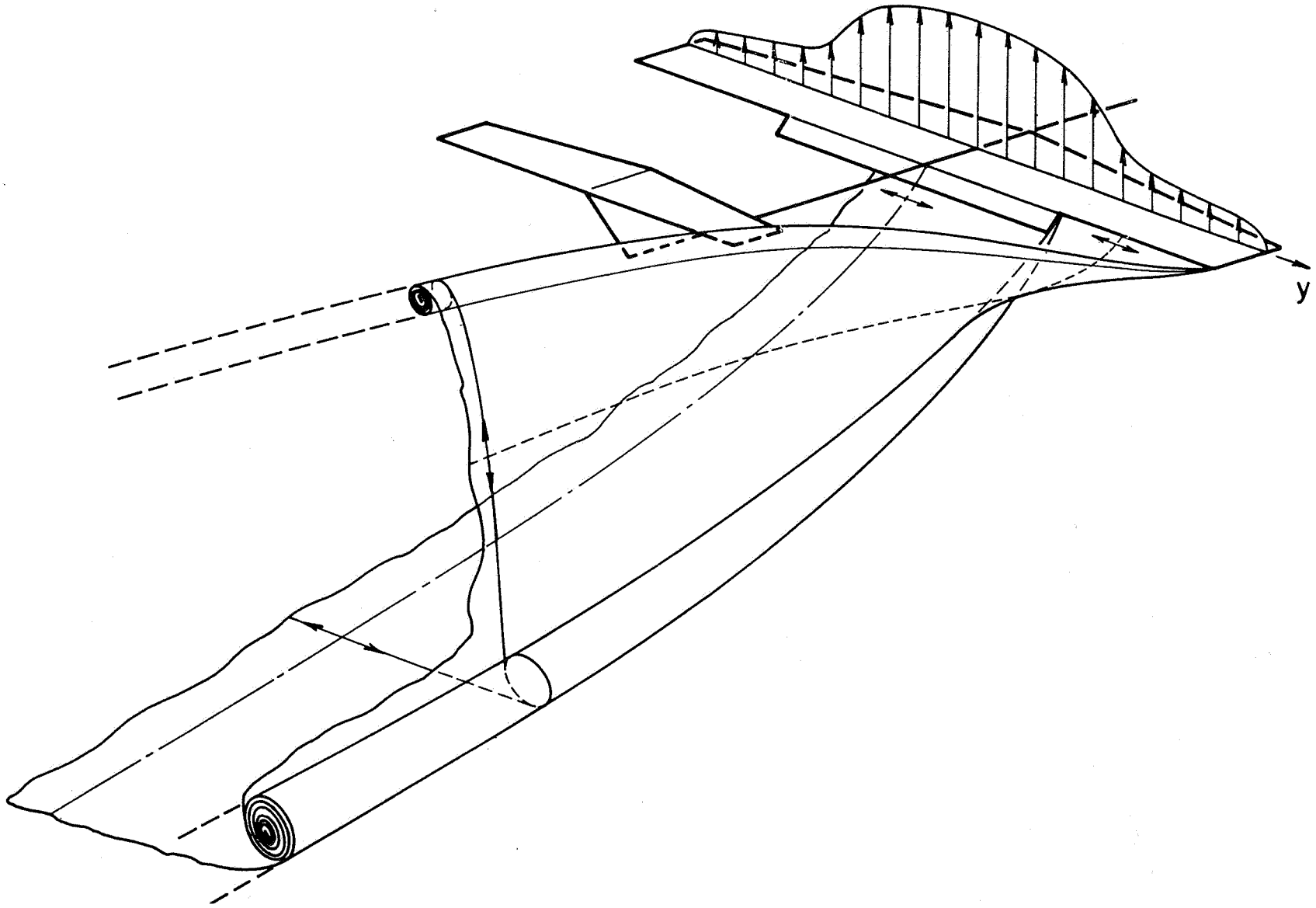

Figure 2. The roll-up of the flap and tip vortices (from ref 6)

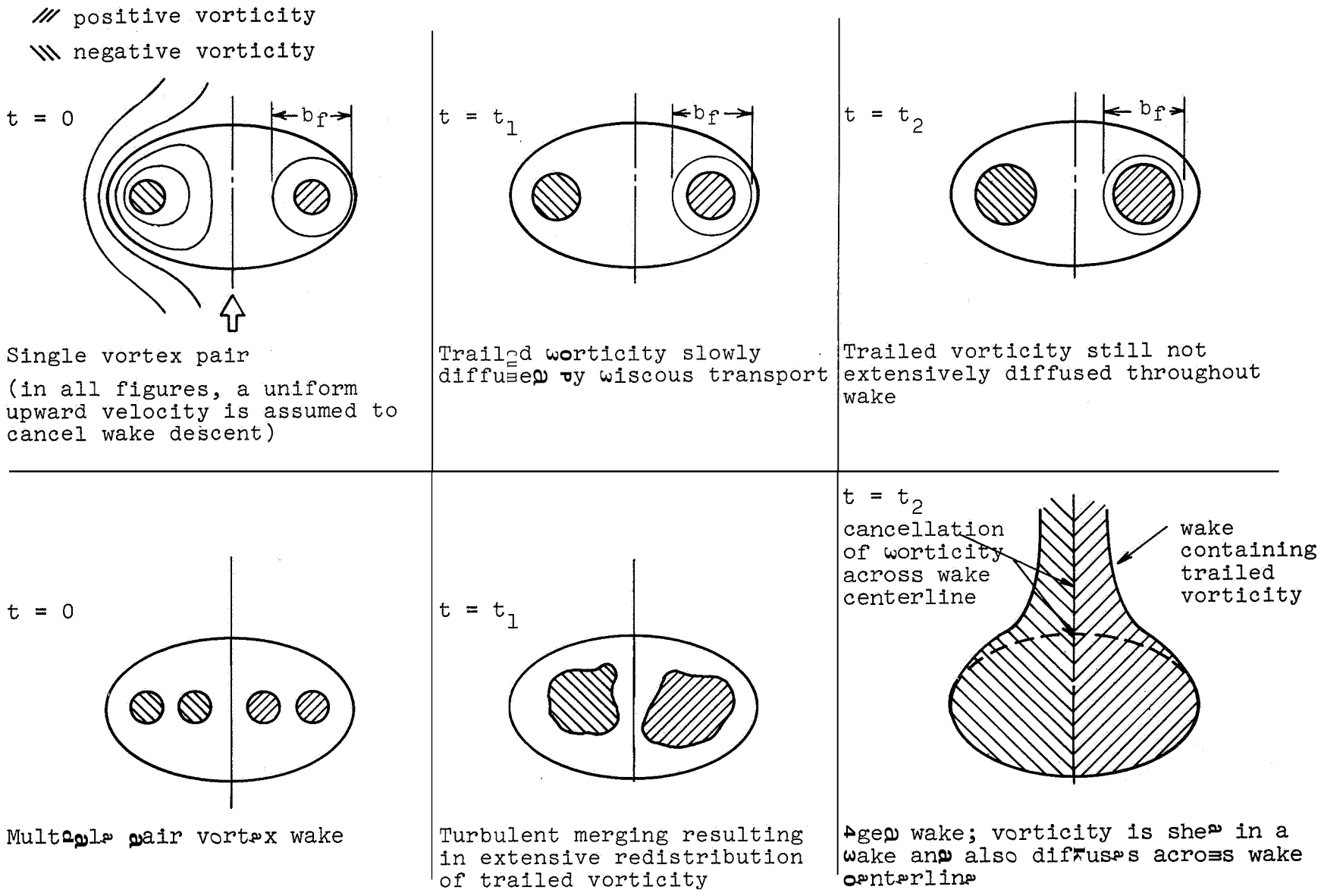

Figure 3. An idealization of the processes which result in the aging of a single- and multiple-pair vortex wake. The encounter aircraft's span is denoted by b_f.

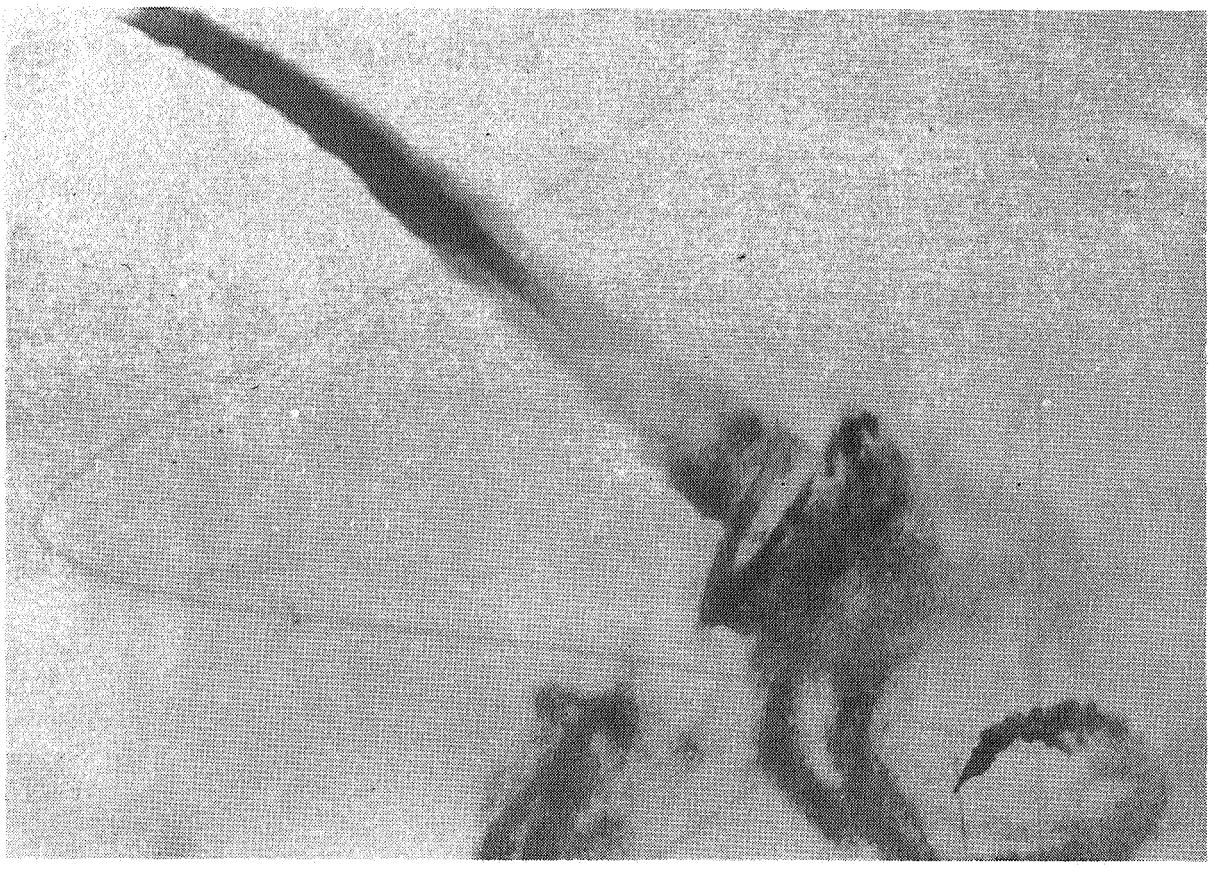

Figure 4. The laminar viscous core of an aircraft vortex. The smoke shows the effect of higher turbulence level in the surrounding atmosphere (ref. 18.

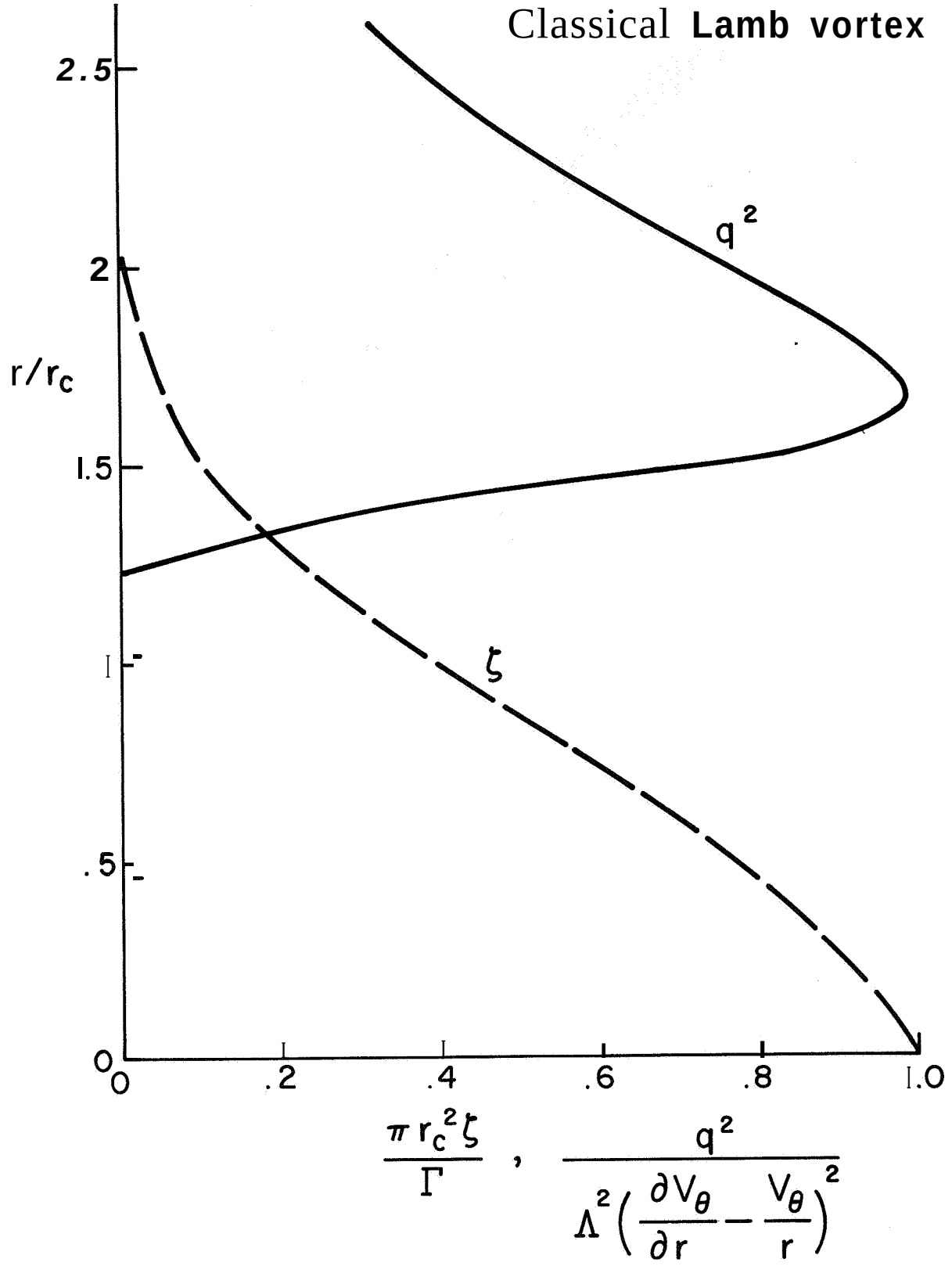

Figure 5. The superequilibrium turbulent kinetic energy and vorticity distribution in a Lamb vortex.

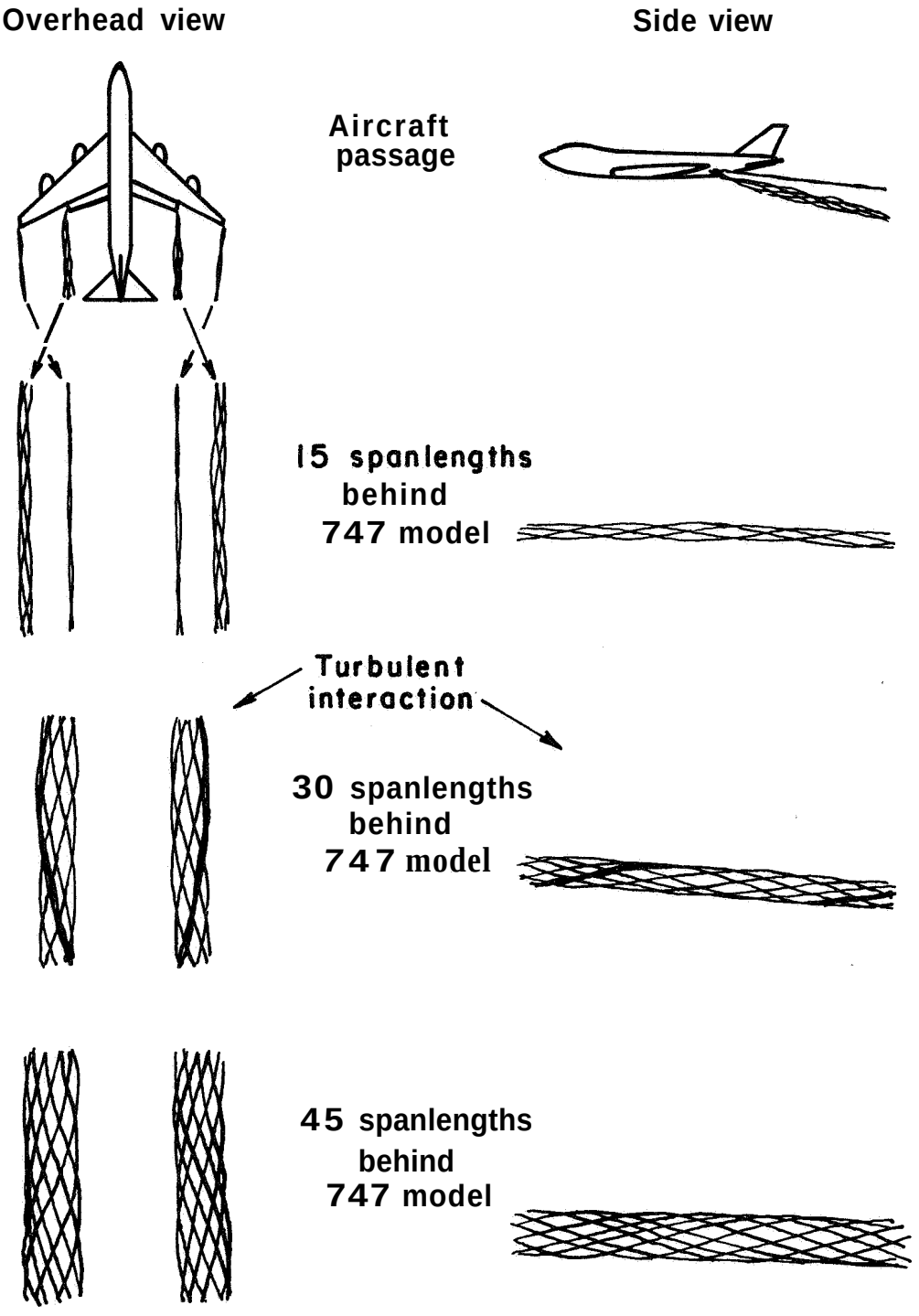

Figure 6. Merging interaction of a tip and a flap vortex as sketched by Dunham (ref. 9).

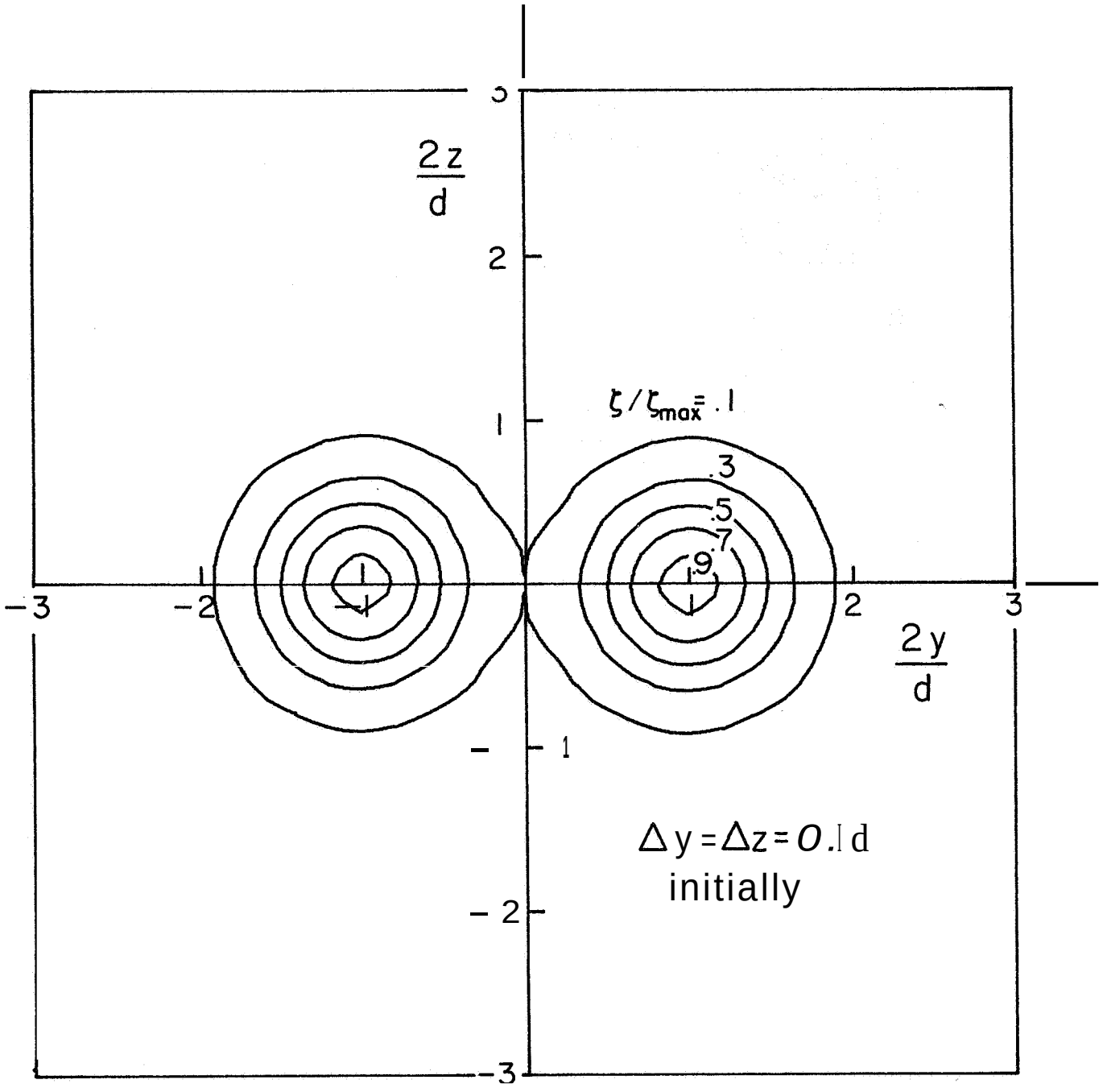

Figure 7. The computational domain and the isopleths of the initial vorticity distribution. The computational boundaries are moved outward as the computation proceeds.

$t\Gamma/\pi d^2 = 0.0$; $P_{min}/P_n = 1.0$

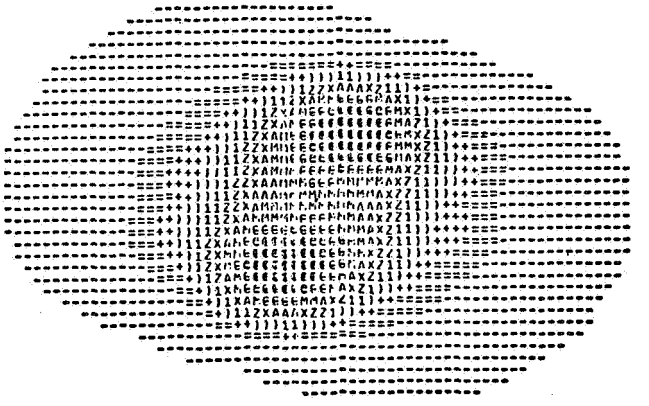

$t\Gamma/\pi d^2 = 1.33$; $P_{min}/P_n = 0.75$

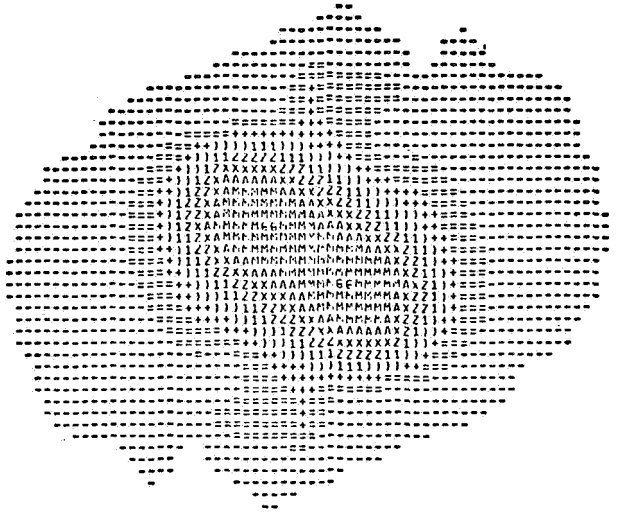

$t\Gamma/\pi d^2 = 2.67$; $P_{min}/P_n = 0.52$

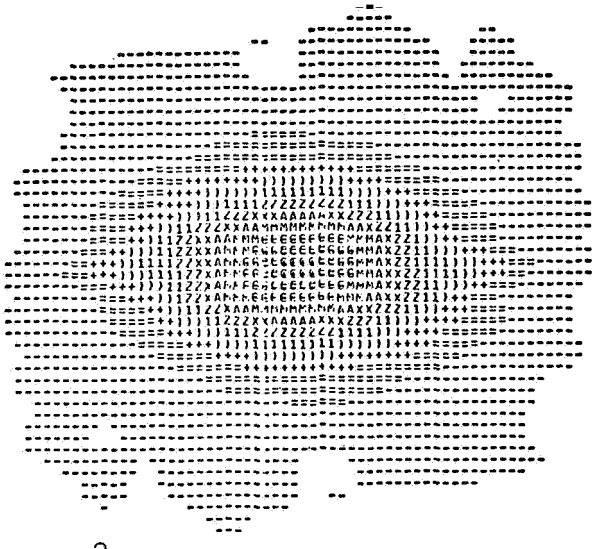

$t\Gamma/\pi d^2 = 4.0$; $P_{min}/P_n = 0.65$

Figure 8. Pressure intensity plots for the merging of two equal strength, like-signed vortices. $P_n = -6.0\rho_o(\Gamma/\pi d)^2$.

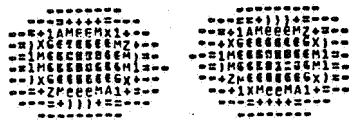

$t\Gamma/\pi d^2 = 0.0$; $\zeta_{max}/\zeta_n = 1.0$

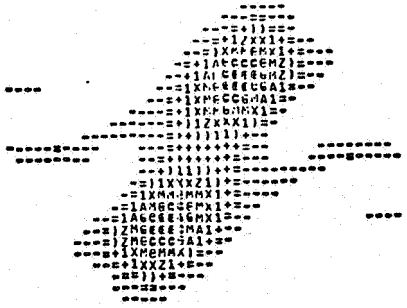

$t\Gamma/\pi d^2 = 1.33$; $\zeta_{max}/\zeta_n = 0.58$

$t\Gamma/\pi d^2 = 2.67$; $\zeta_{max}/\zeta_n = 0.35$

$t\Gamma/\pi d^2 = 4.0$; $\zeta_{max}/\zeta_n = 0.34$

Figure 9. Vorticity intensity plots for the merging of two equal strength, like-signed vortices. $\zeta_n = 14.8\Gamma/\pi d^2$.

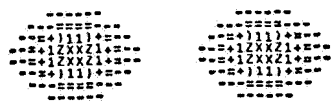

$t\Gamma/\pi d^2 = 0.0$; $q^2_{max}/q^2_n = 0.18$

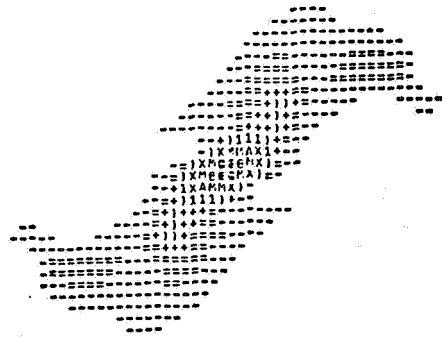

$t\Gamma/\pi d^2 = 1.33$; $q^2_{max}/q^2_n = 0.3$

$t\Gamma/\pi d^2 = 2.67$; $q^2_{max}/q^2_n = 0.52$

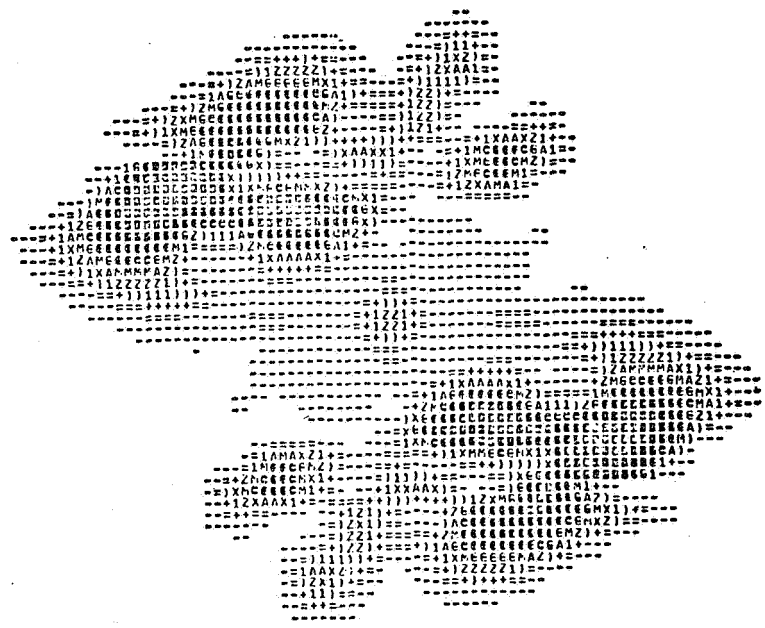

$t\Gamma/\pi d^2 = 4.0$; $q^2_{max}/q^2_n = 1.0$

Figure 10. Turbulent kinetic energy intensity plots for the merging of two equal strength, like-signed vortices. $q^2_n = 0.54(\Gamma/\pi d)^2$.

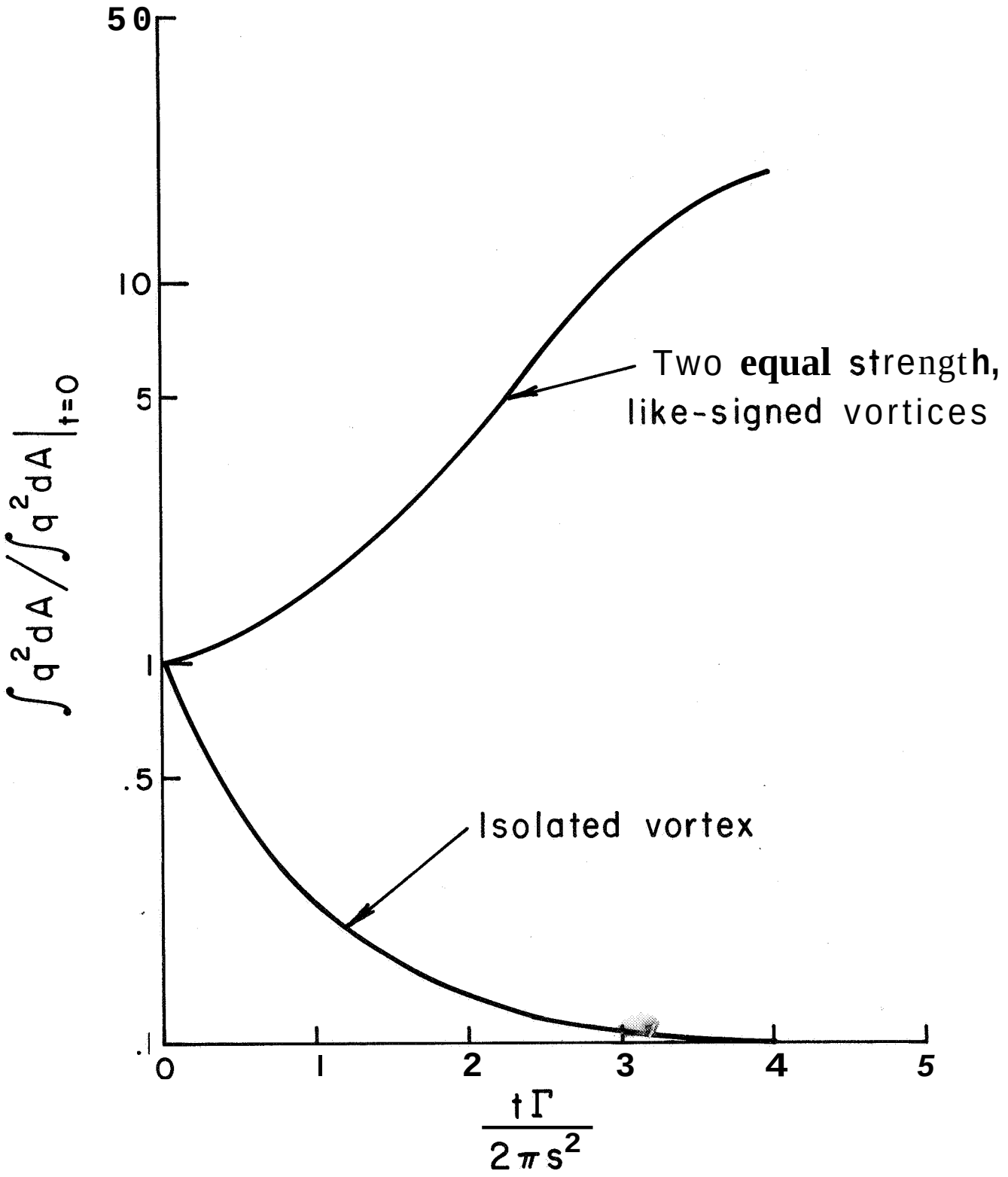

Figure 11. Comparison of the turbulent kinetic energy as a function of time between an isolated vortex and two equal strength, like-signed vortices.

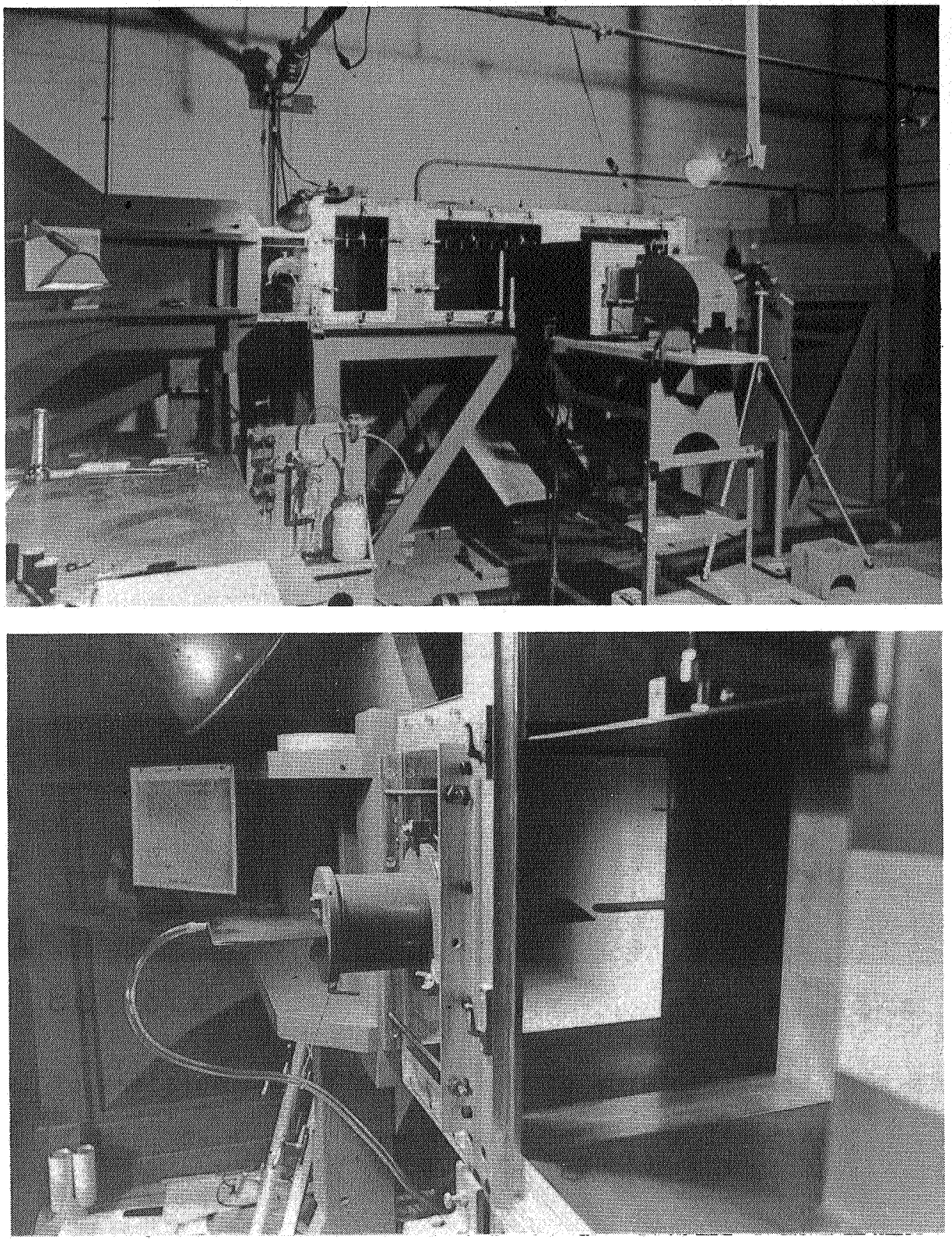

Figure 12. View of the A.R.A.P. wind tunnel (top) and the vortex generator airfoils (bottom).

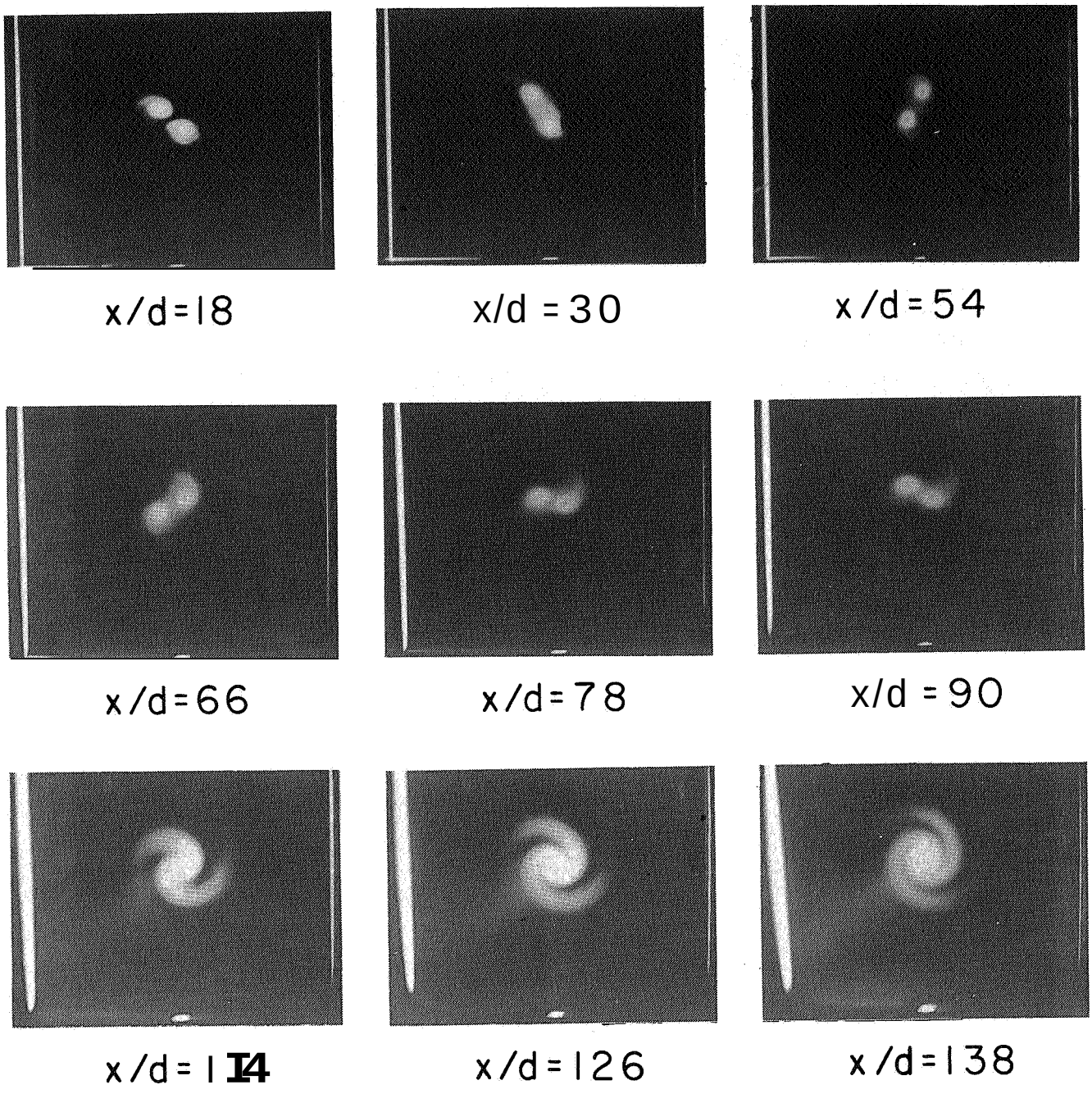

Figure 13. Smoke pictures of the merging of two vortices of like sign and strength at several downstream locations. The airfoil angles of attack are $\alpha_{left} = -6°$ and $\alpha_{right} = +6°$ and the tip spacing d = 1.27 cm.

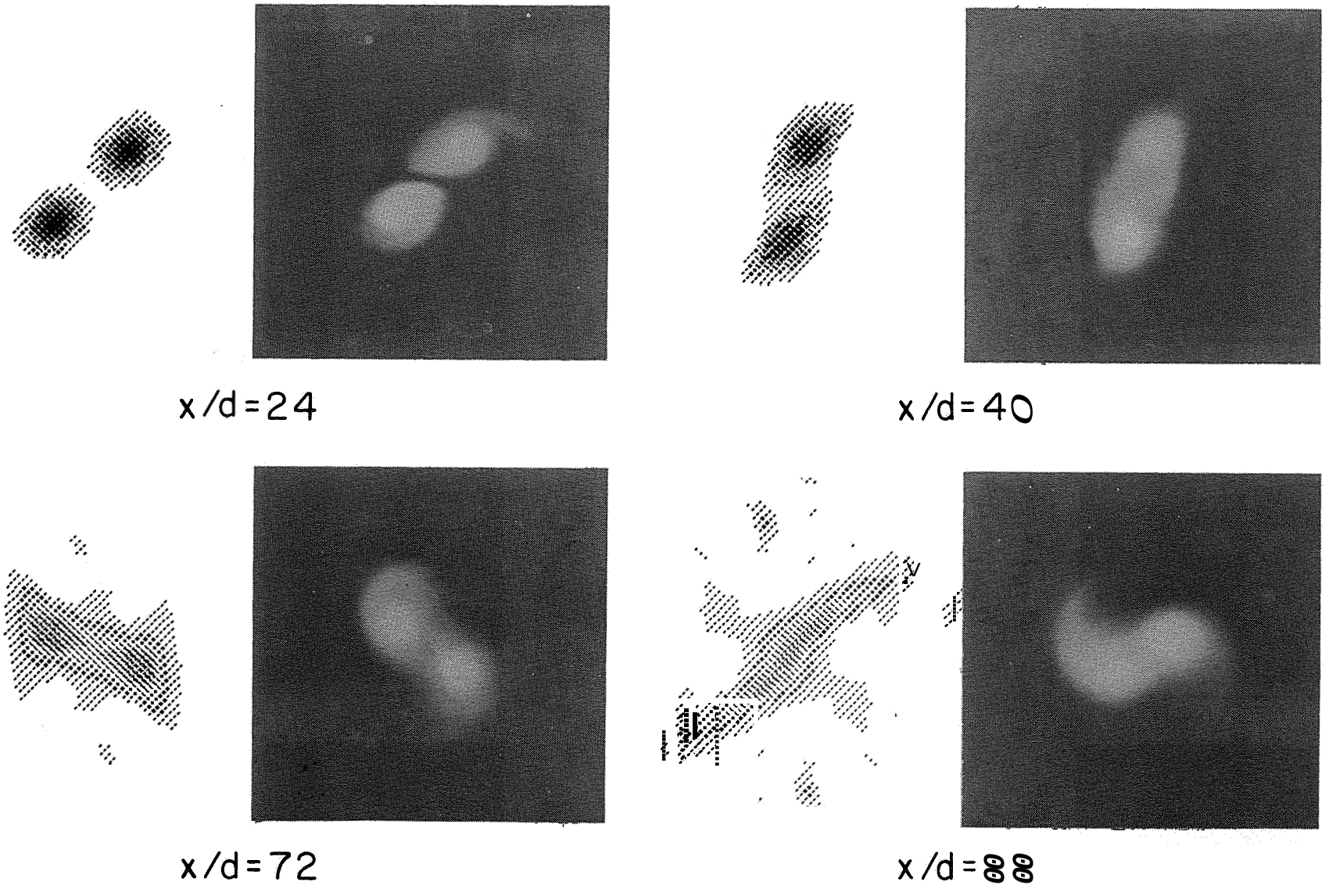

Figure 14. Comparisons of computed merging of vorticity distributions with smoke patterns in vortices of like sign and strength. The airfoil angles of attack are $\alpha_{left} = +6°$ and $\alpha_{right} = -6°$. The tip spacing d = 0.95 cm.

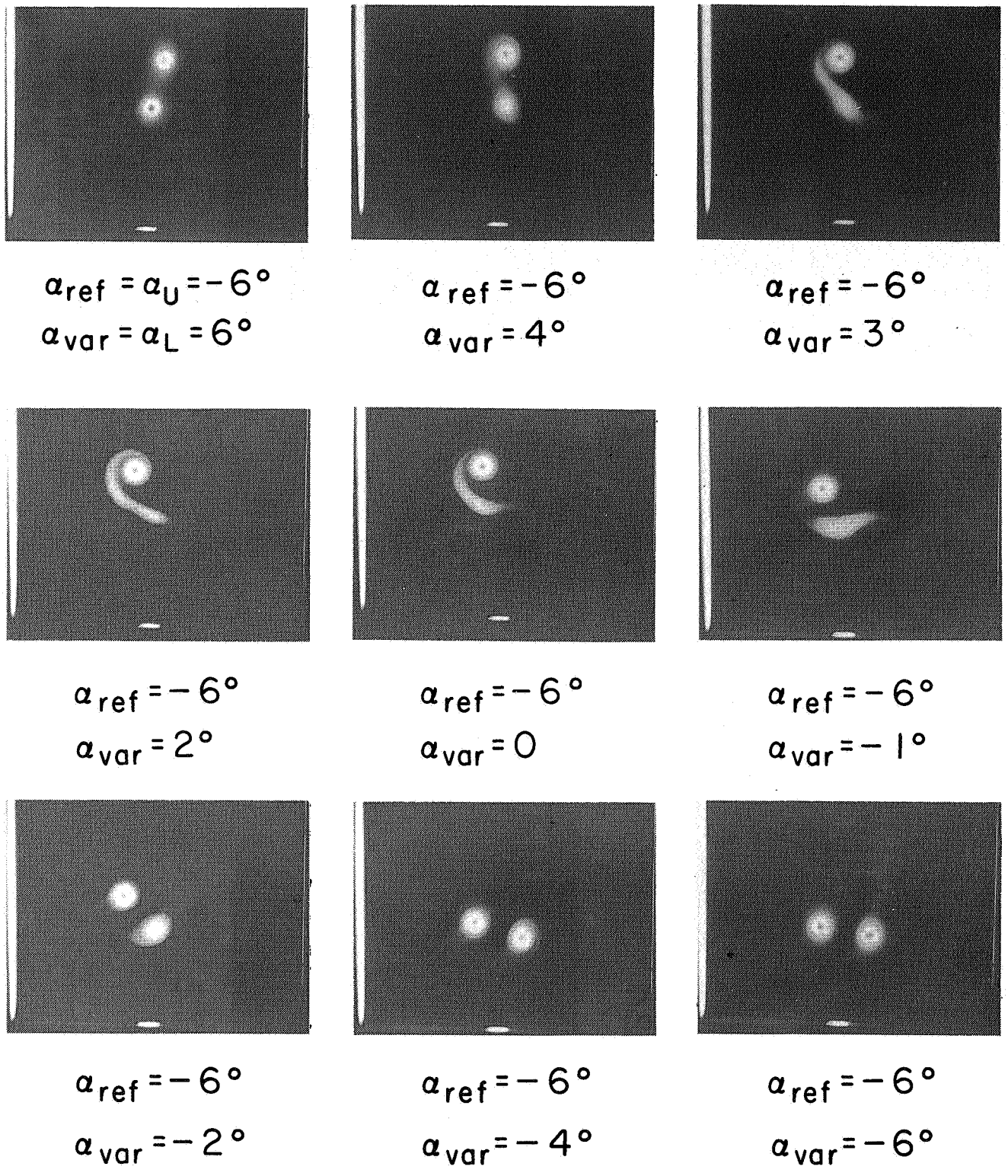

Figure 15. Smoke pictures of the interaction of one vortex of constant strength with another of varying strength and sign. The axial station is x/d = 55.4 and the tip spacing d = 2.06 cm.

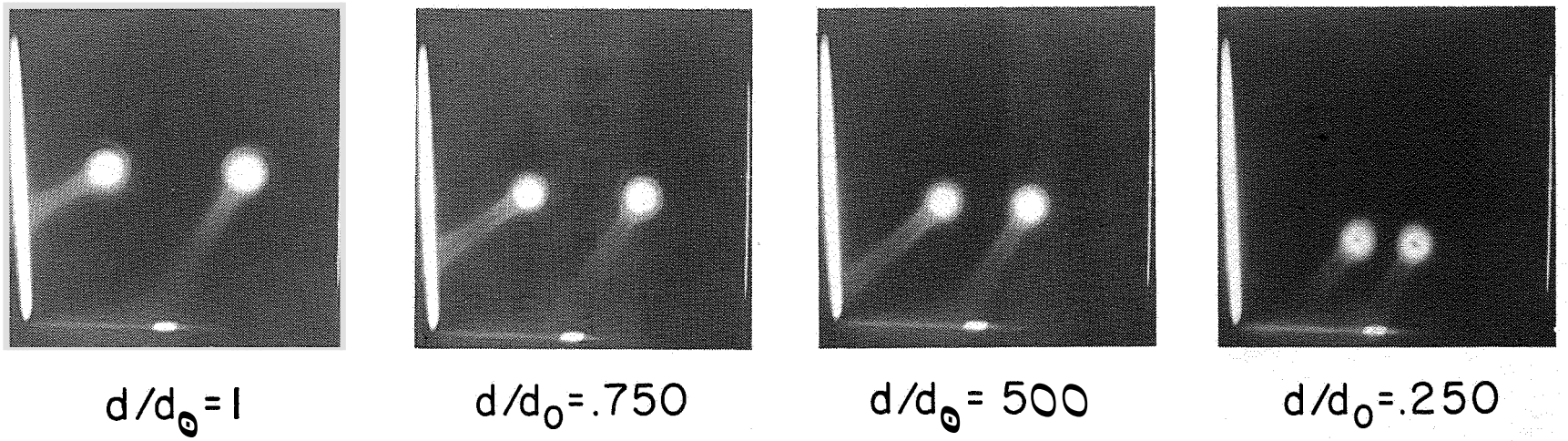

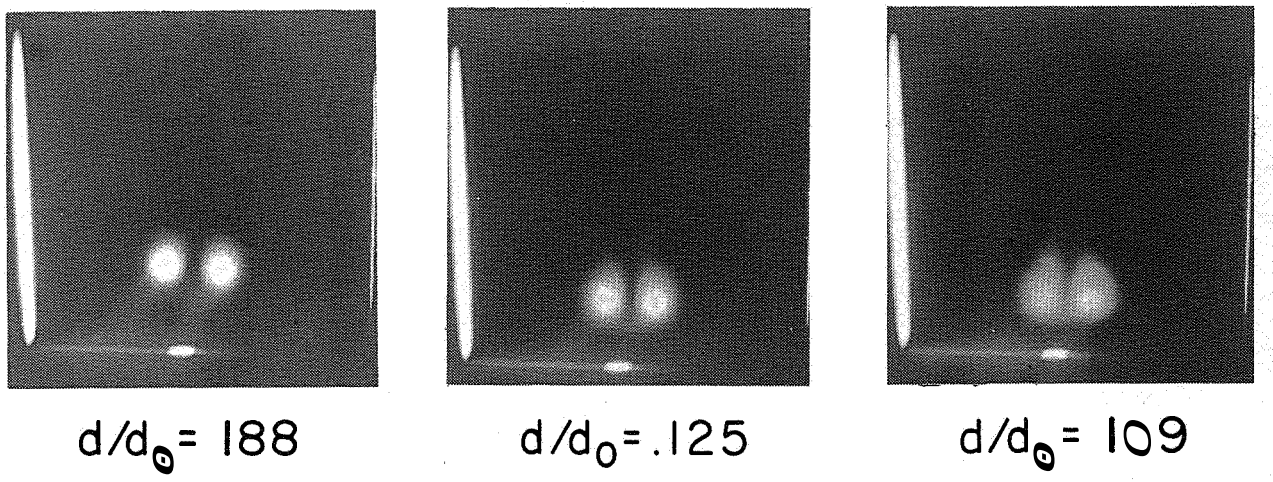

Figure 16 Smoke pictures of a pair of vortices of opposite sign and equal strength. Both airfoils are set at $\alpha = -6°$ and the axial station $x/d_o = 15.75$. The initial tip spacing $d_o = 10.16$ cm.

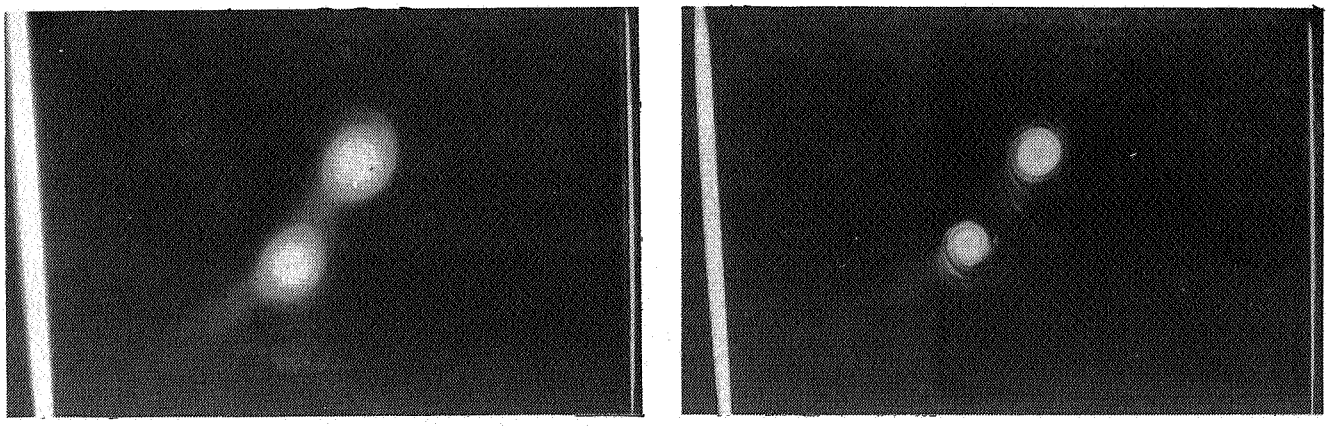

d=2.54 cm, x/d=63
Continuous illumination

d=2.54 cm, x/d=63
Flash illumination

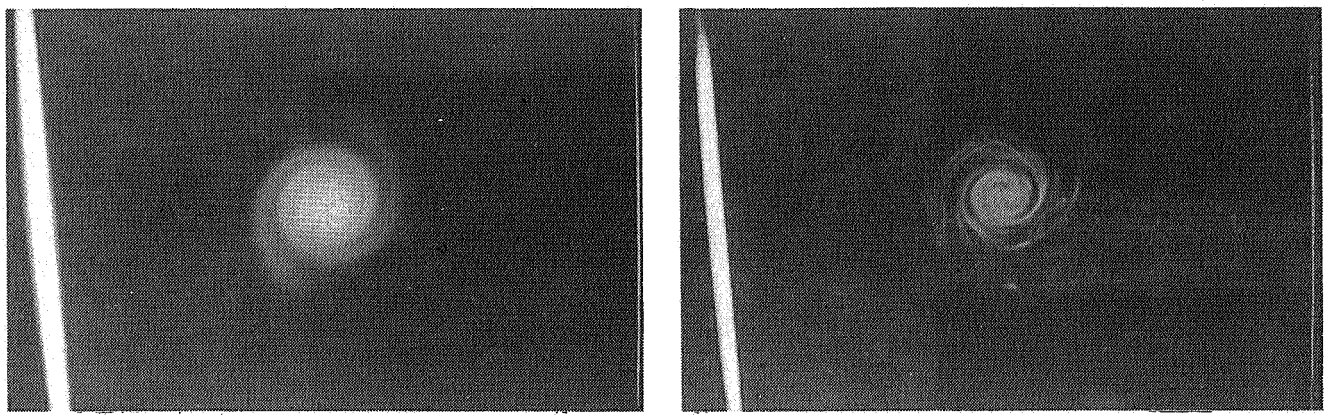

d=0.95 cm, x/d=184
Continuous illumination

d=0.95 cm, x/d=184
Flash illumination

Figure 17. Illustrations of the smoke patterns under continuous (1/2 sec exposure, left) and flash (1/2800 sec exposure, right) illumination.

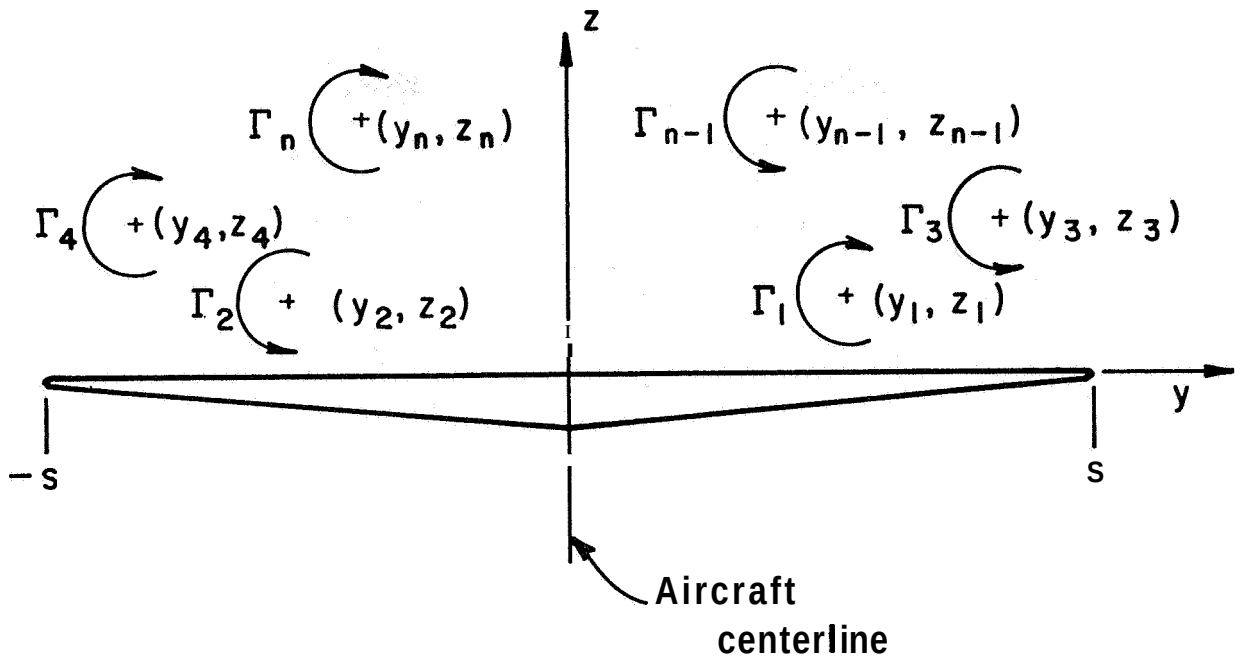

Figure 18. Geometry for the calculation of the downstream location of vortex centroids.

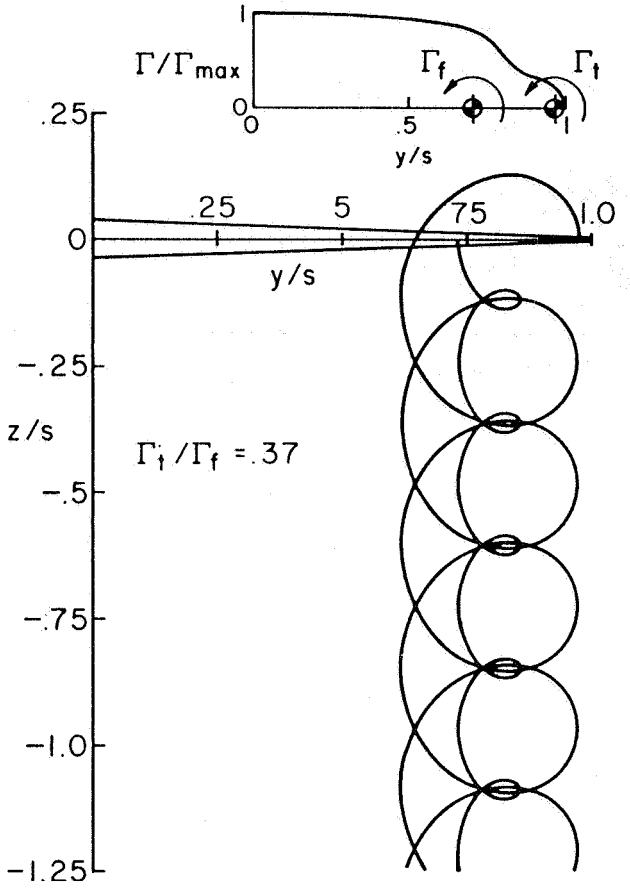

Figure 19. Vortex centroid locations as seen from downstream with strong interaction between neighboring vortices (ref. 6).

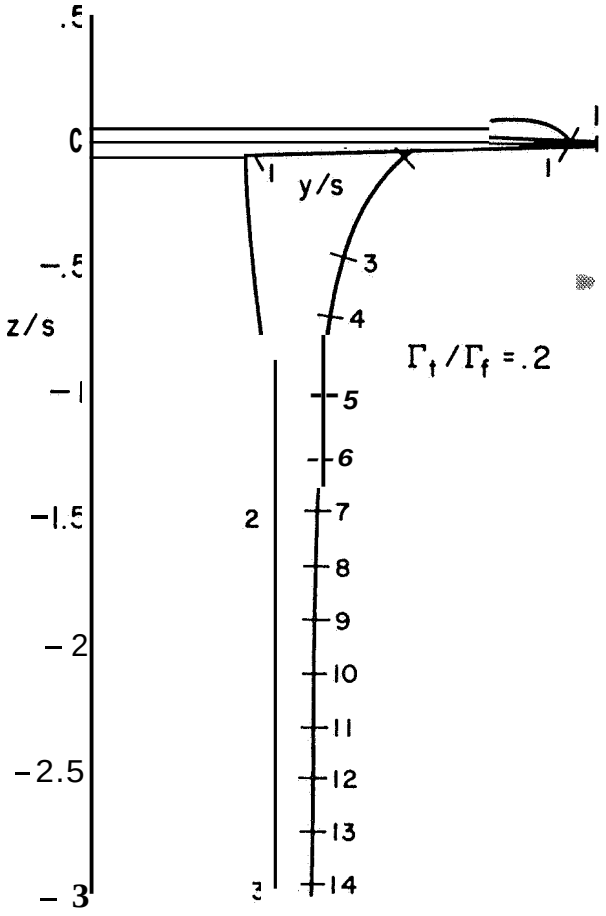

Figure 20. Vortex centroid locations as seen from downstream with weak interaction between like-signed vortices - pairs diverge. The time interval between consecutive integers is a constant (ref. 6).

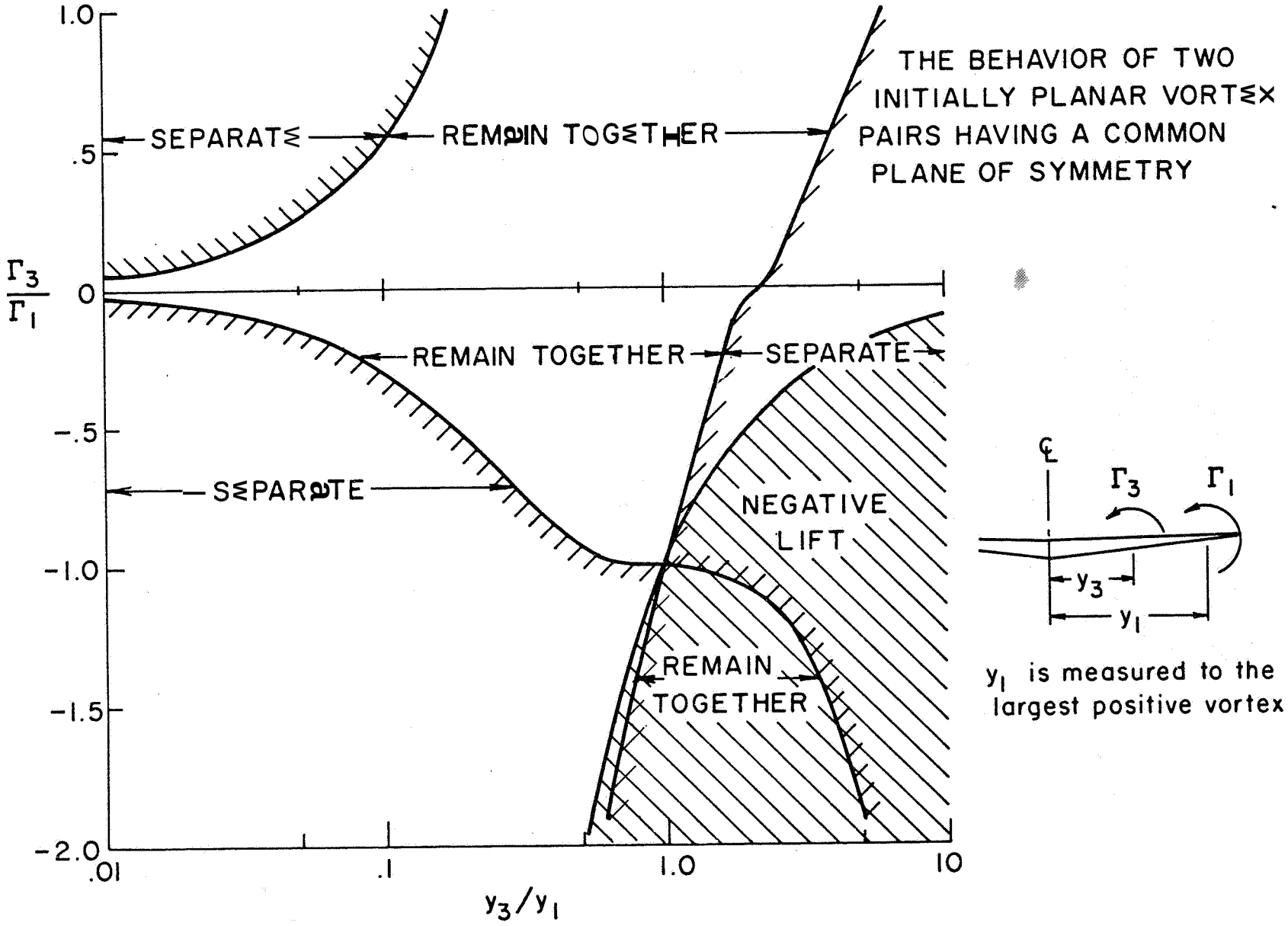

Figure 21. Wake classification chart for two-vortex-pair wakes

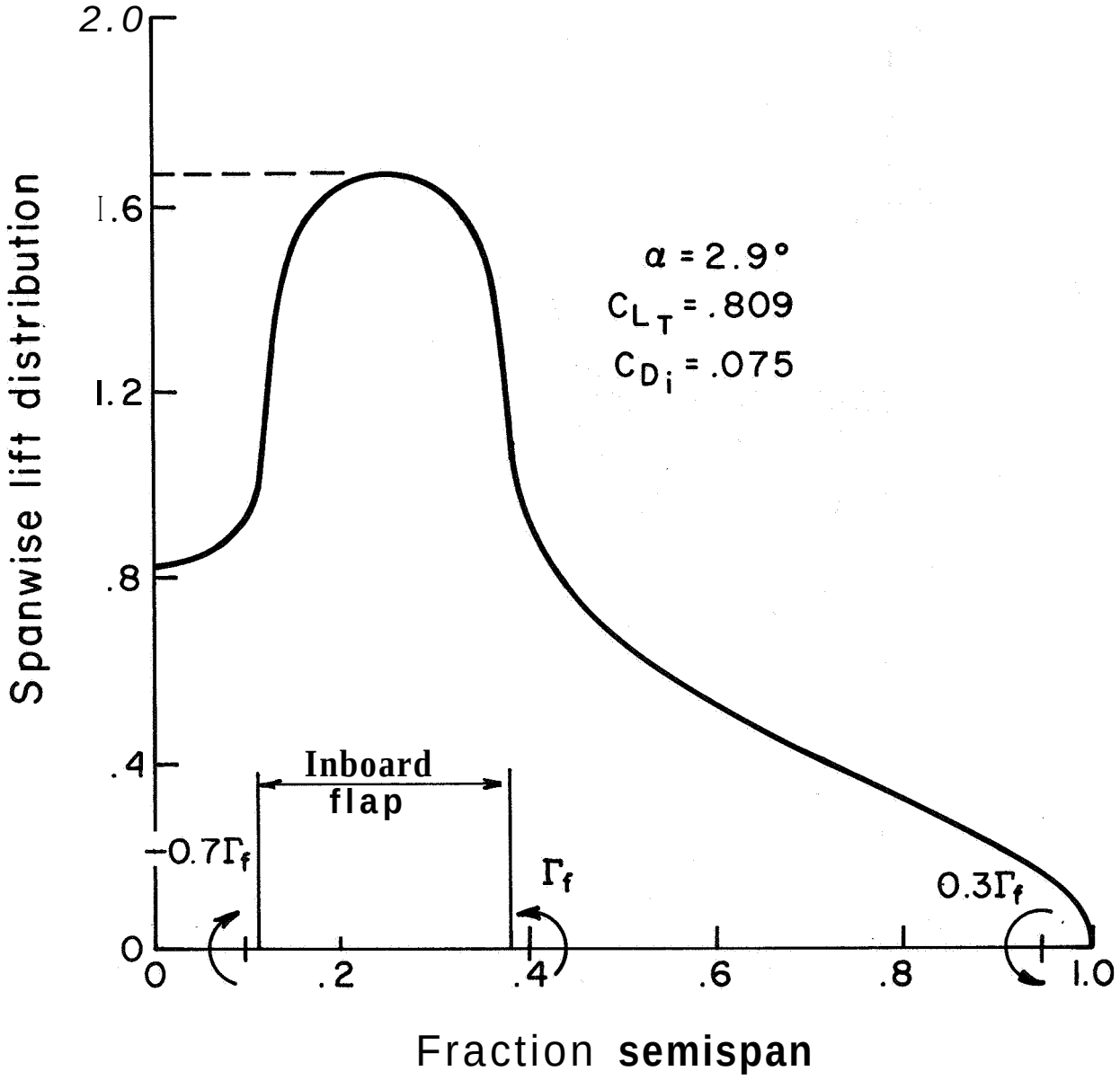

Figure 22. Predicted spanwise lift distribution; LDG/O configuration (ref. 16).

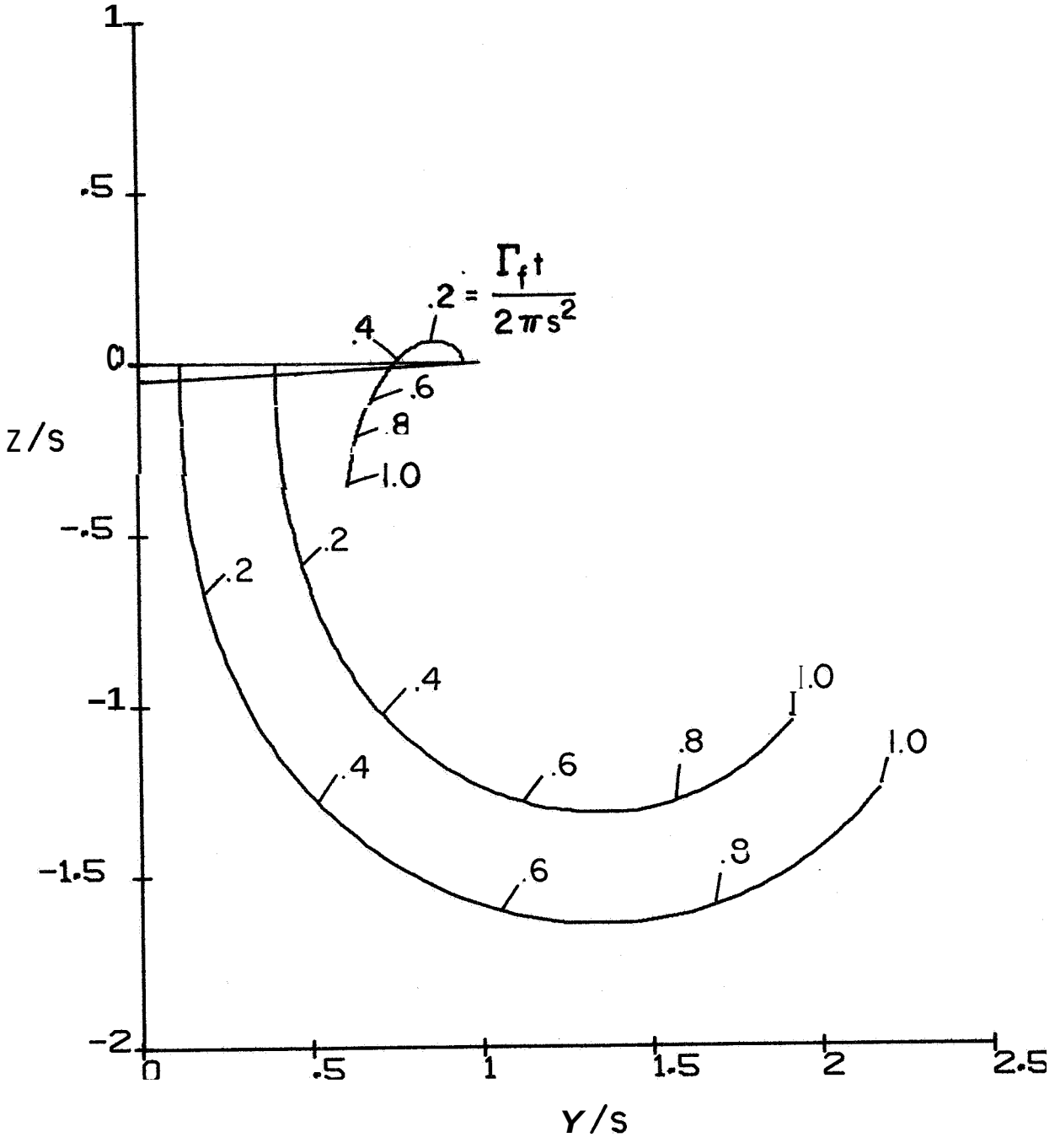

Figure 23. Trajectories of the centroids of discrete vortices generated by the LDG/O configuration (see fig. 22).

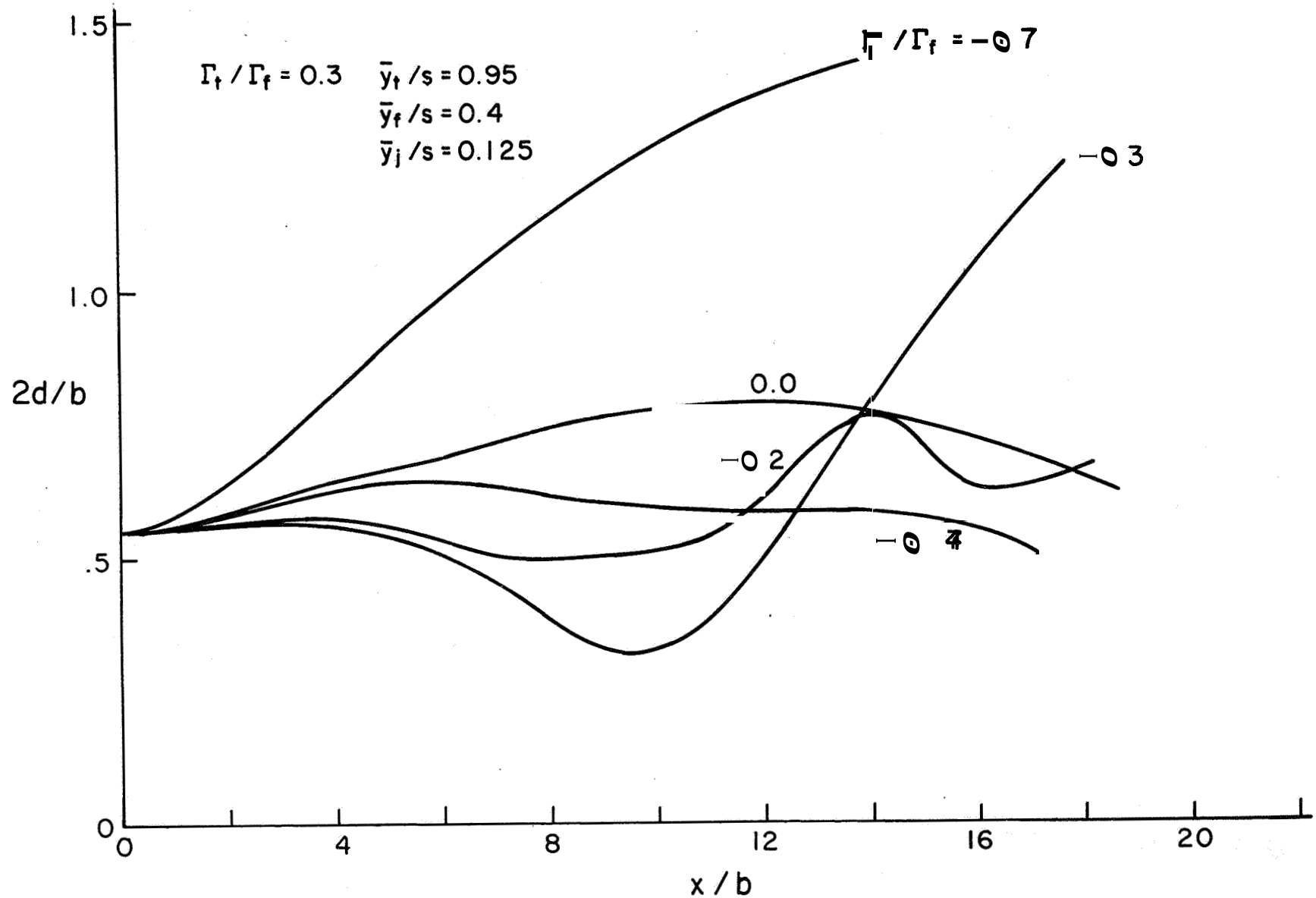

Figure 24. Sensitivity of the separation between tip and flap vortices as a function of the strength of the fuselage vortex Γ_j . The results for the LDG/O configuration shown in figure 22 are labeled $\Gamma_j = -0.7\Gamma_f$.

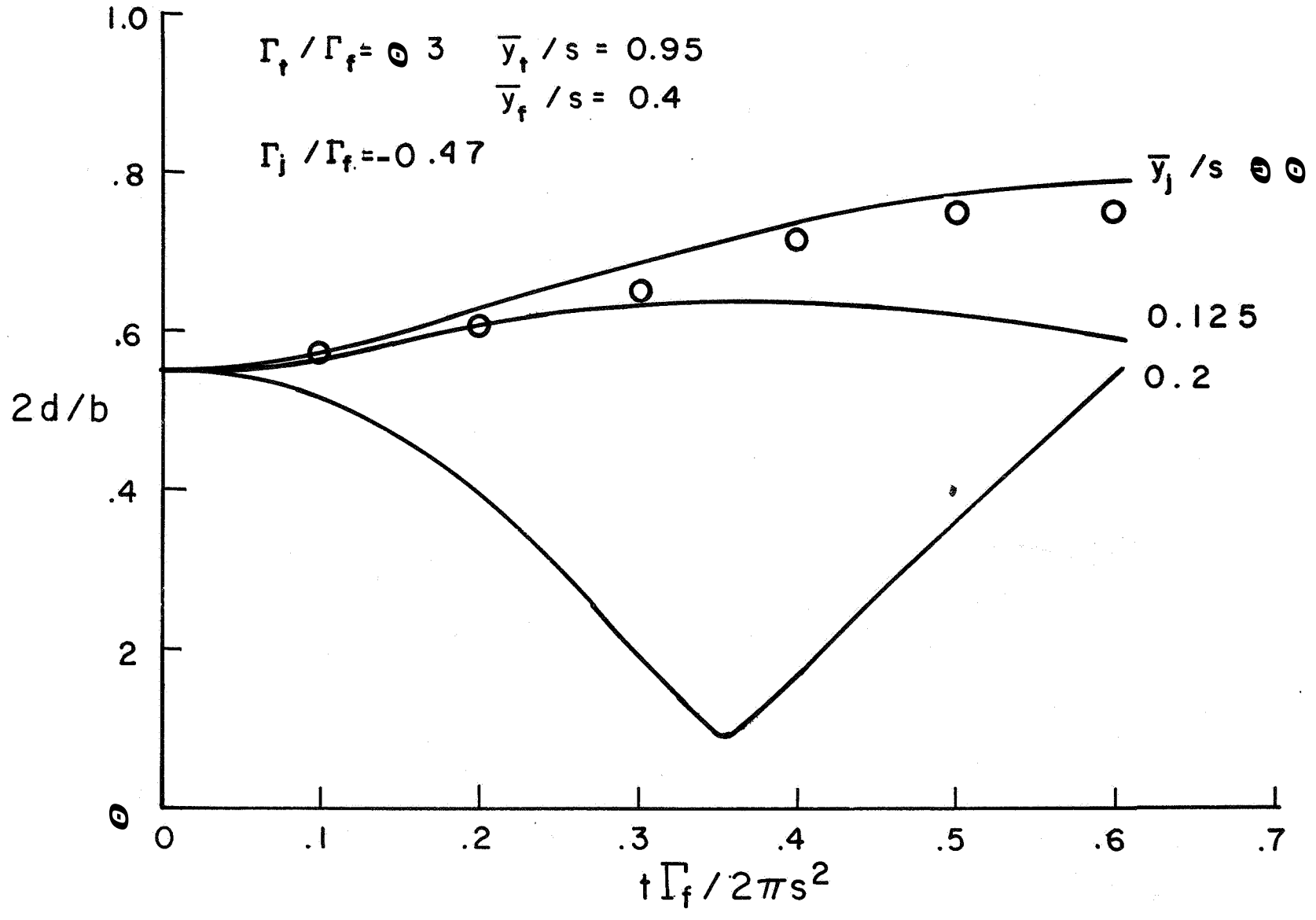

Figure 25. Sensitivity of the separation between tip and flap vortices as a function of the initial position of the fuselage vortex $\bar{y}_j$.

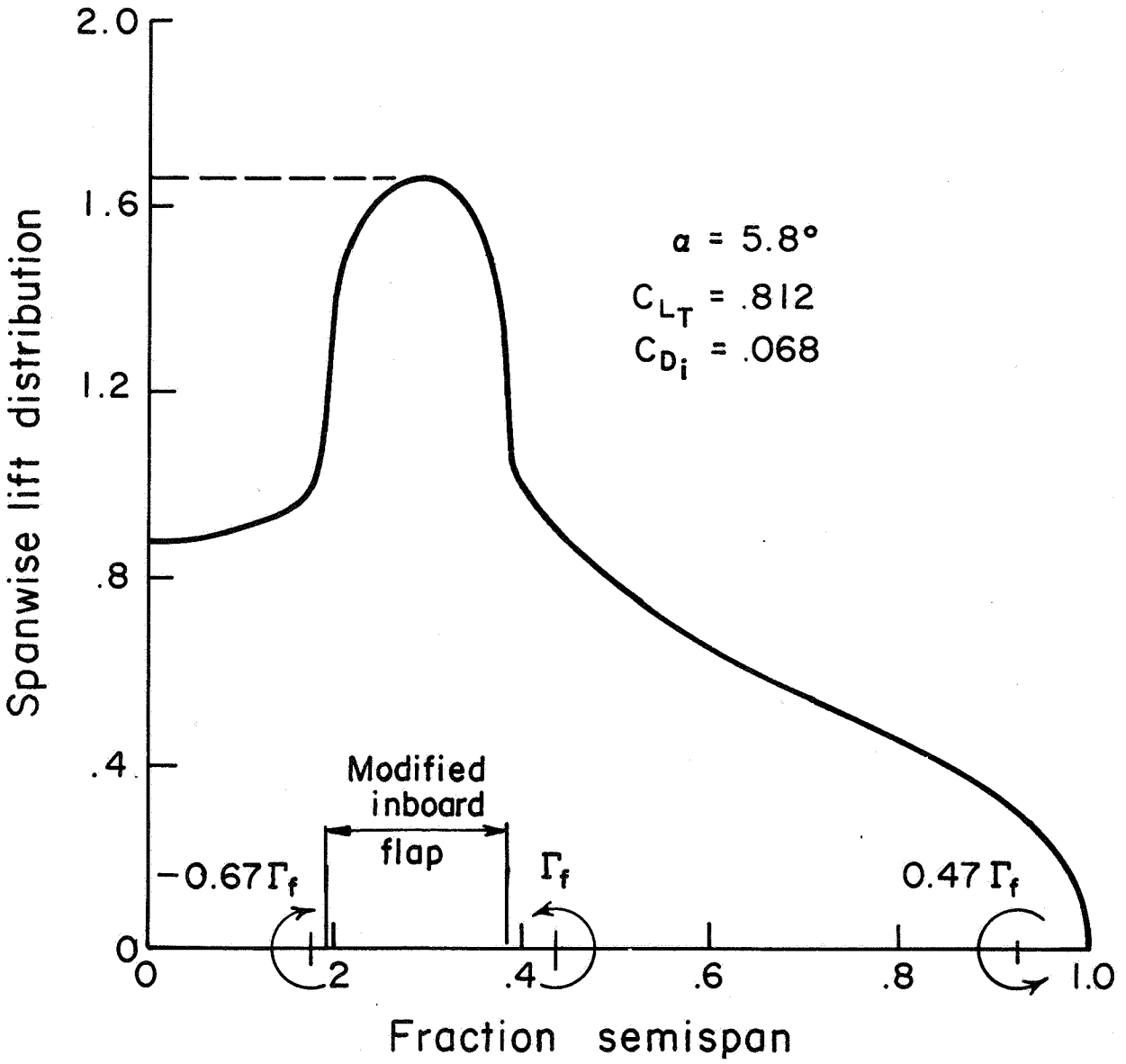

Figure 26. Predicted spanwise lift distribution, modified LDG/O configurations (ref. 16)

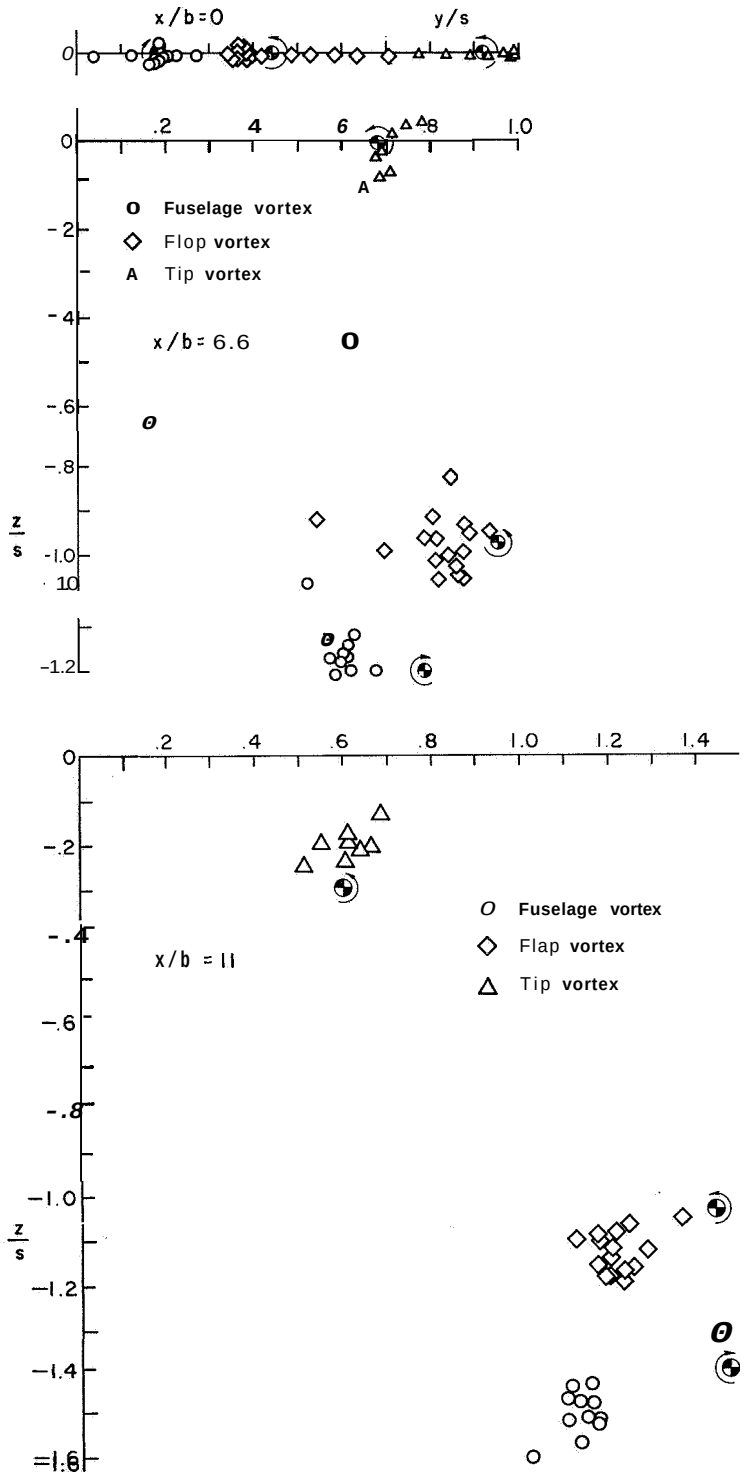

Figure 27. Comparison between using forty point vortices to represent the trailed sheet of vorticity and using three point vortices located at +,he centroid of the tip, flap, and fuselage vortices as shown in figure 26. ◒ denotes centroid computed from the three-vortex computation.

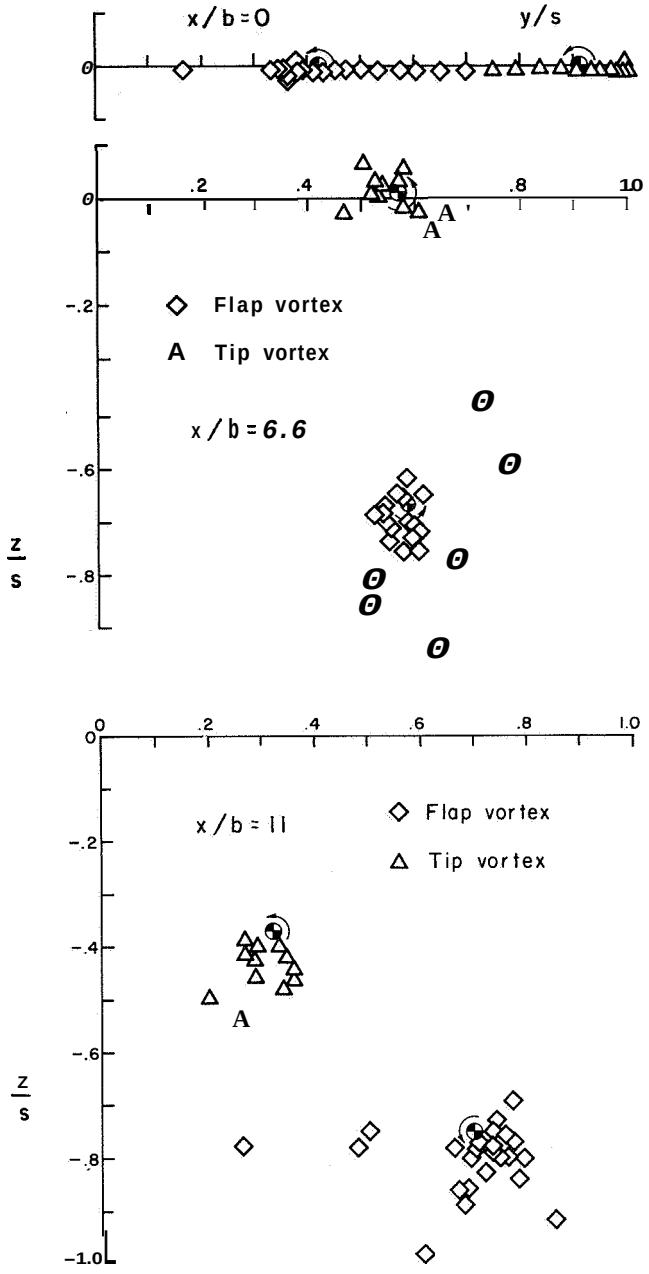

Figure 28. Comparison between using forty point vortices to represent the trailed sheet of vorticity and using two point vortices located at the centroid of the tip and flap vortices as shown in figure 26 (the fuselage vortex has been removed). ◕ denotes centroid computed from the two-vortex computation.

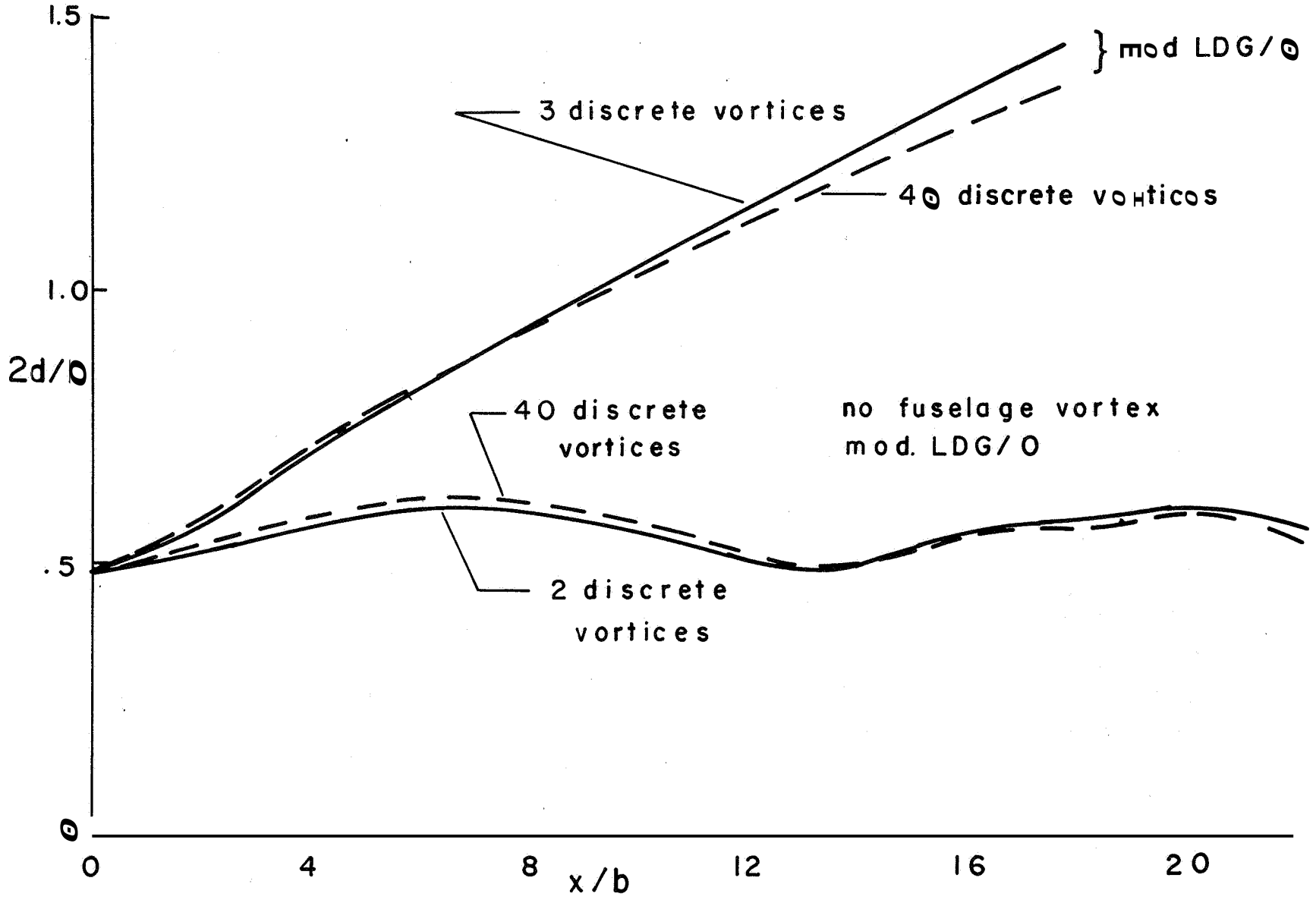

Figure 29. Comparison of the spacing between flap and tip vortices for the mod LDG/0 configuration shown in figure 26.

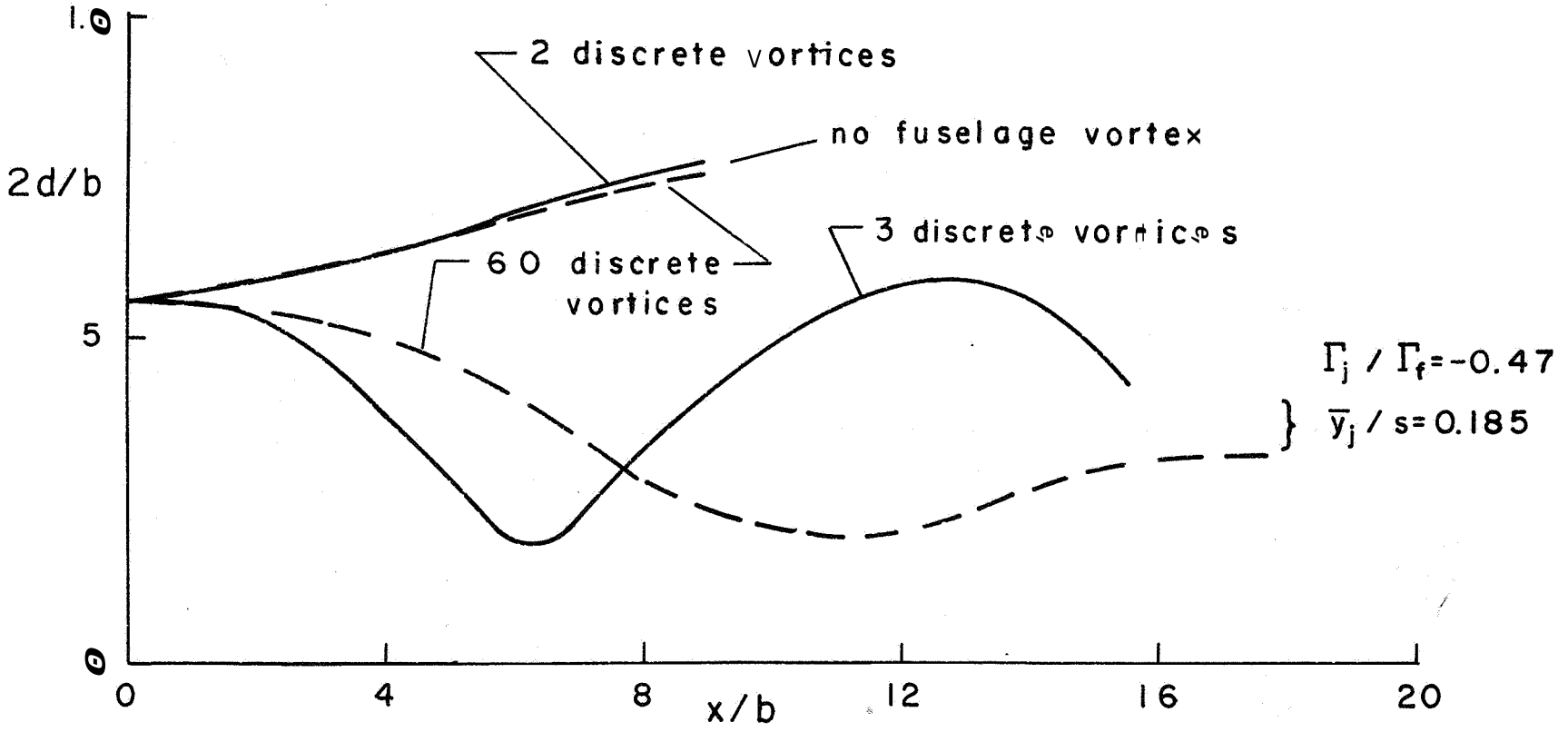

Figure 20 Comparison of the spacing between flap and tip vortices for an inboard altered LDG/O lift distribution.

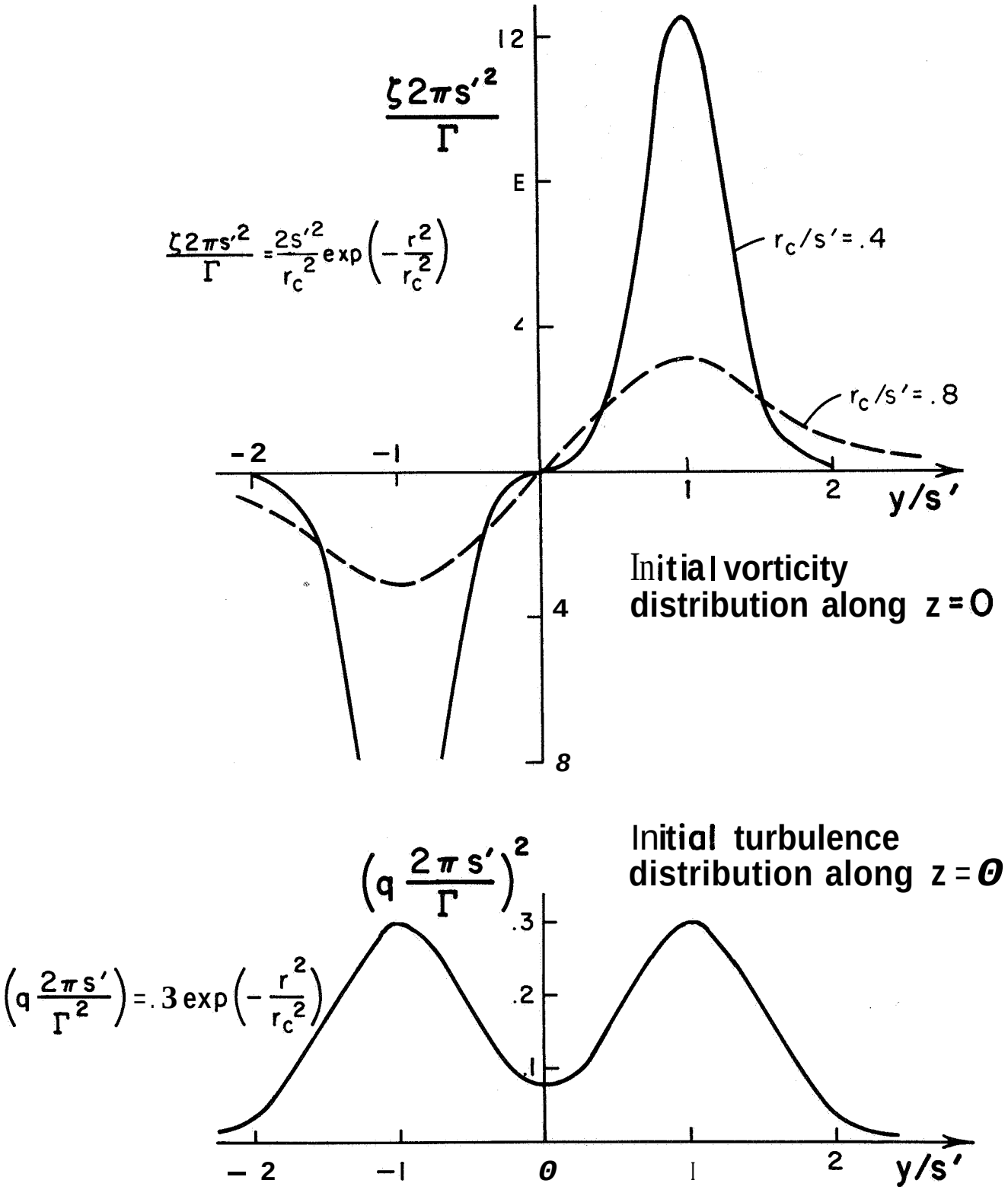

Figure 31. Initial vorticity and turbulent kinetic energy distributions used in the computation of the decay of a vortex pair in a quiescent atmosphere,

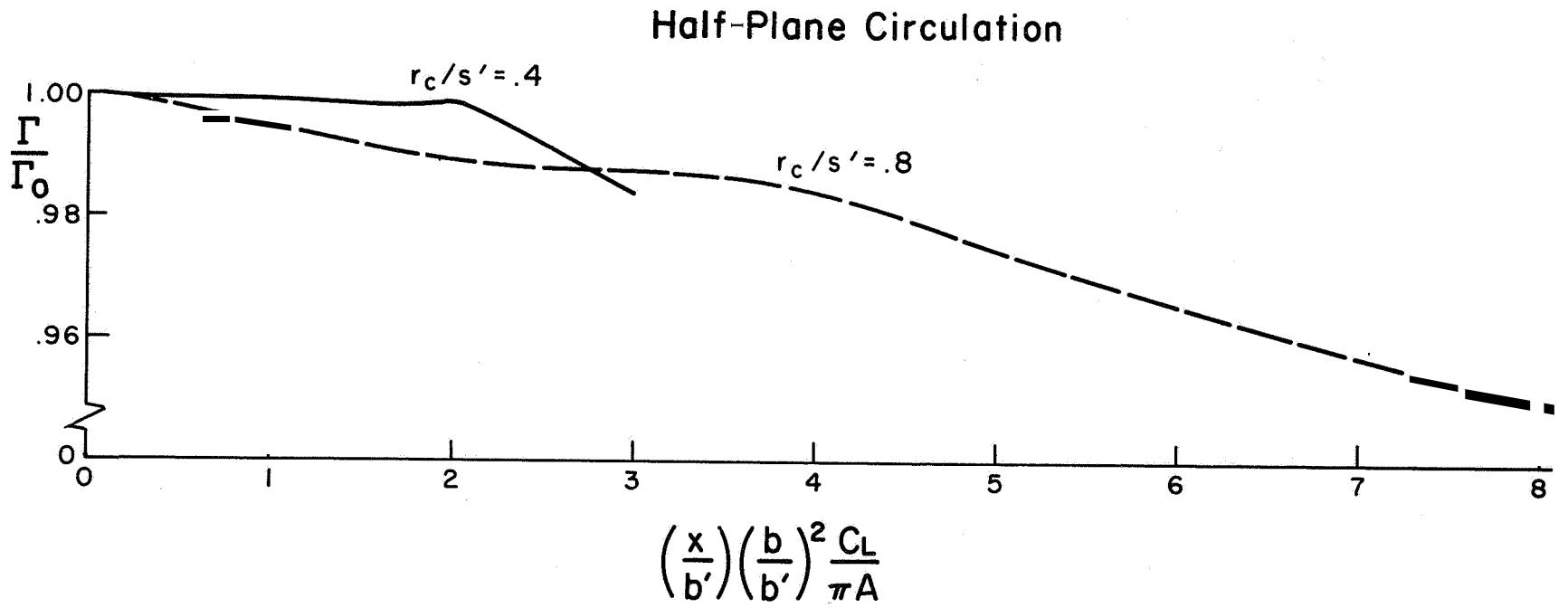

Figure 32. Comparison of the decay of circulation in a counter-rotating vortex pair for two different initial vortex core radii.

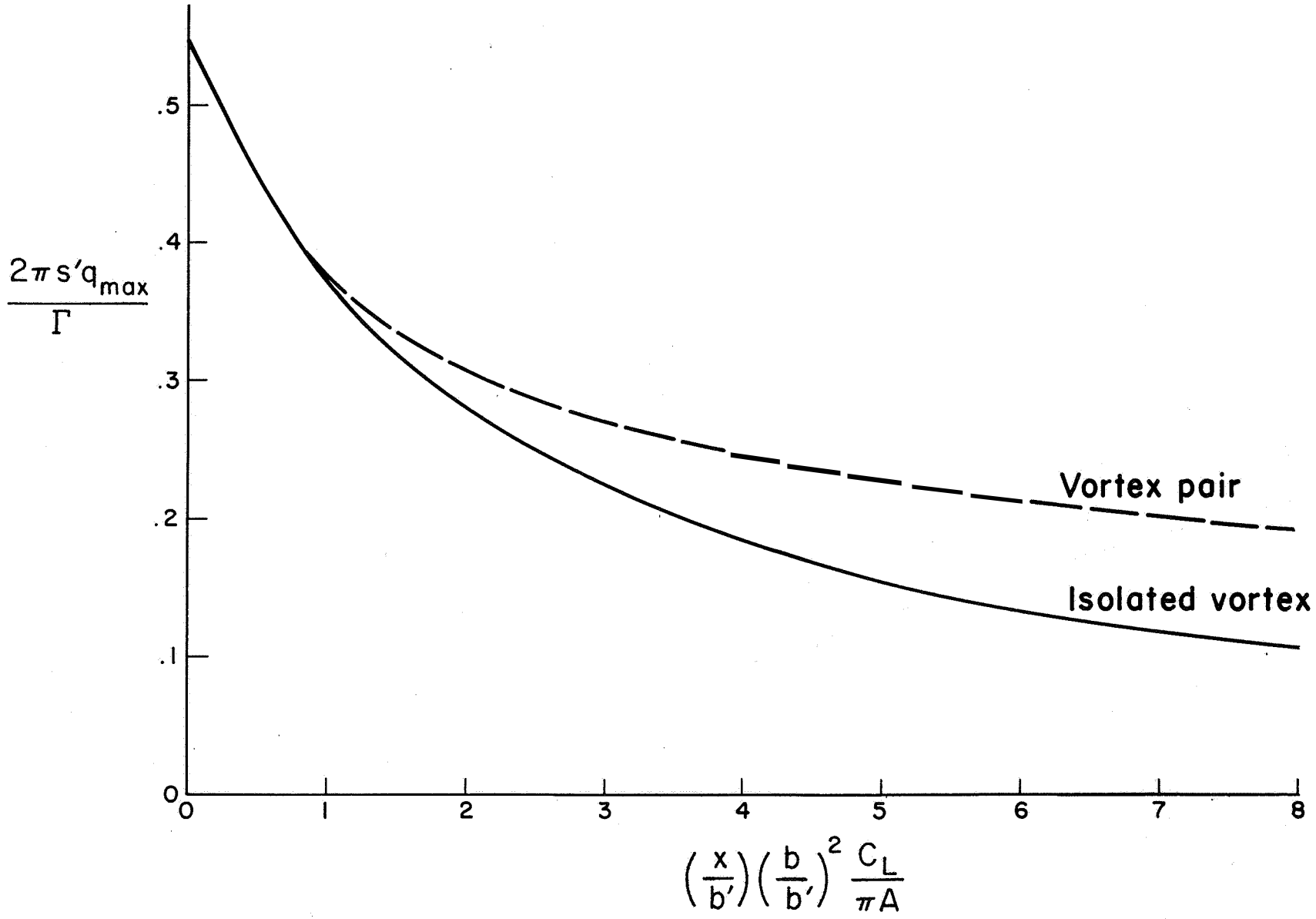

Figure 33 Comparison of the maximum root-mean-square turbulence level in a counter-rotating vortex pair and in an equivalent isolated vortex ($r_c/s' = 0.8$).

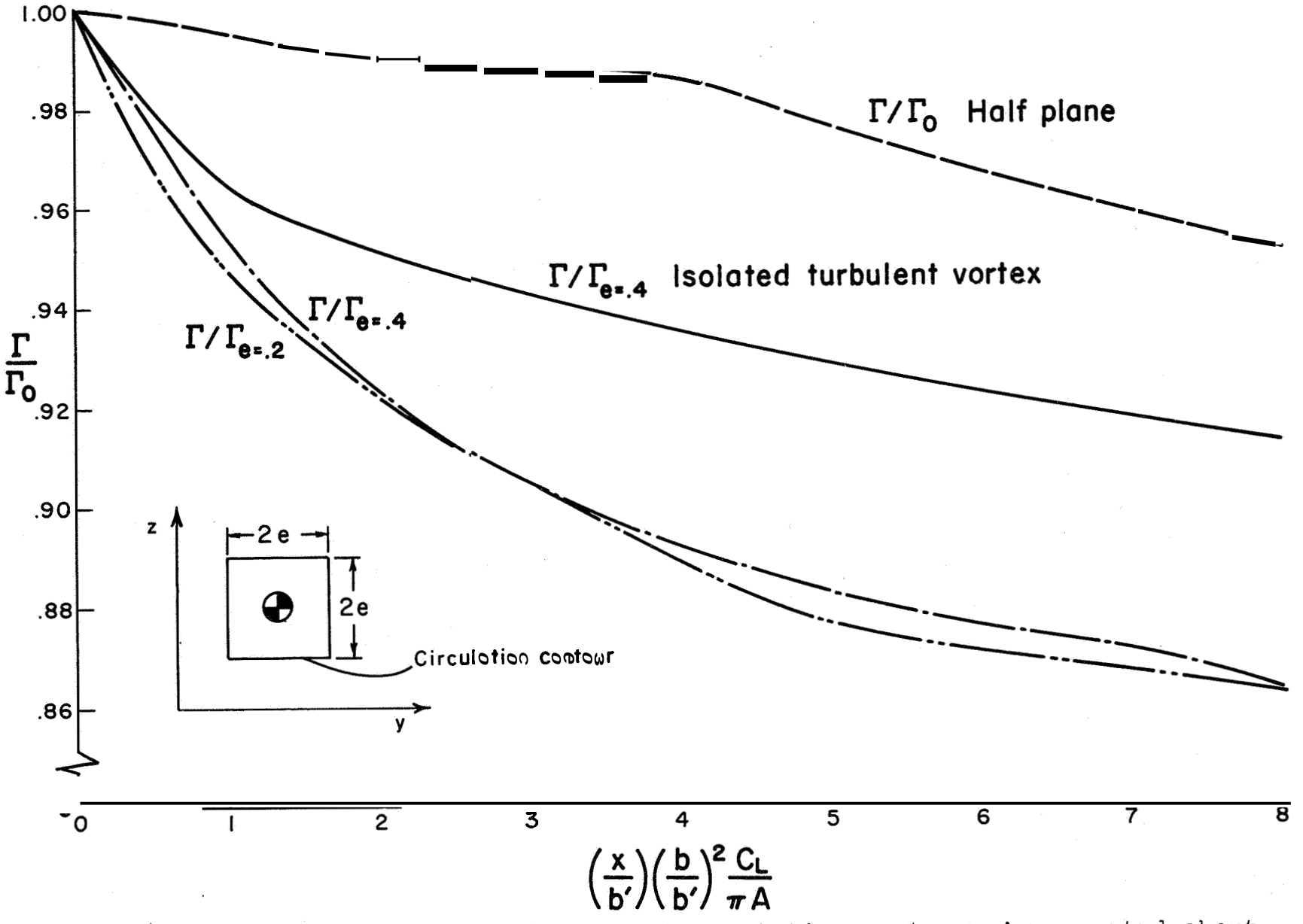

Figure 34. Decay of circulation in a counter-rotating vortex pair computed about square contours centered at the centroid of vorticity of the half-plane vorticitv distribution ($r_c/s' = 0.8$).

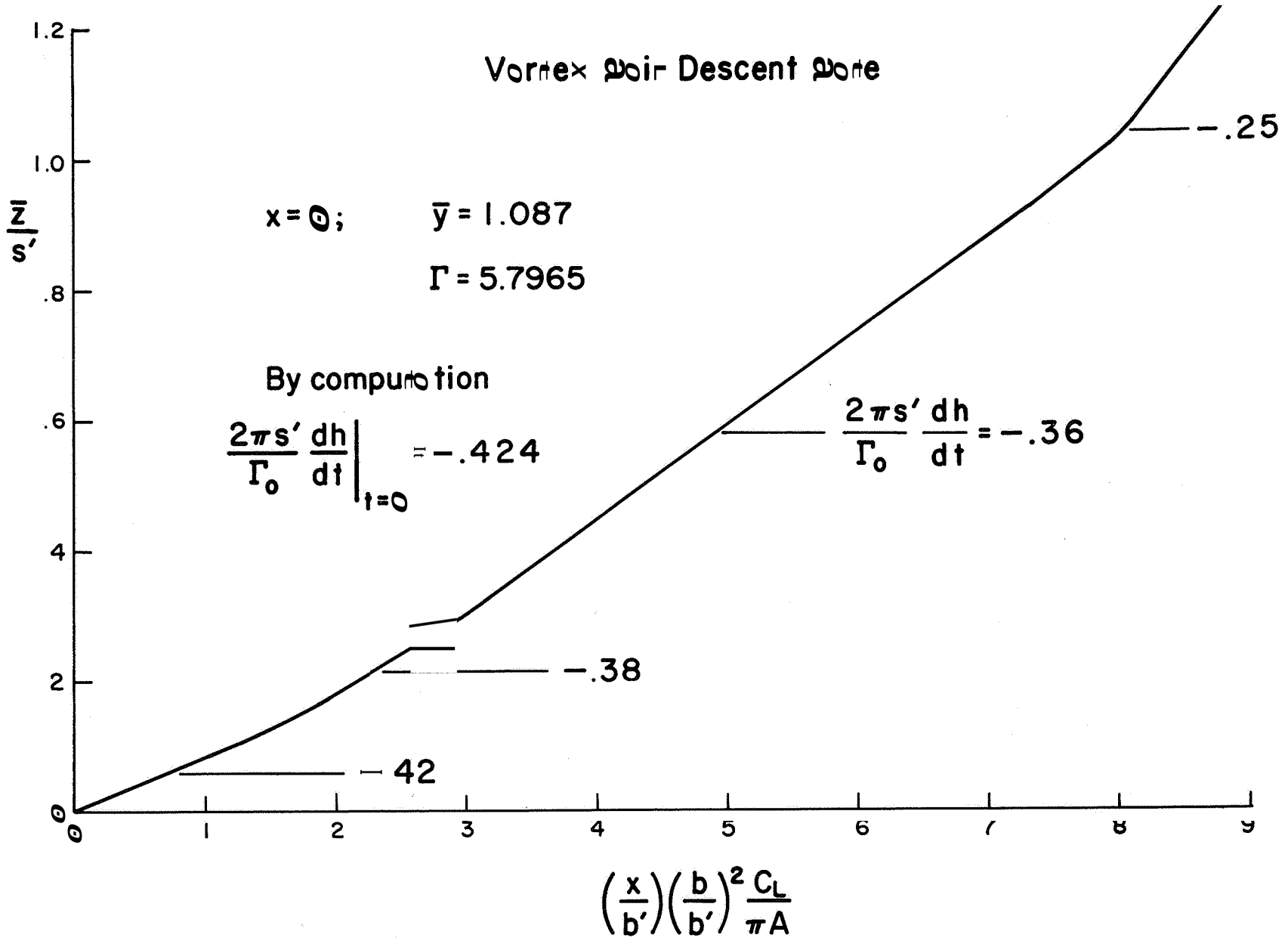

Figure 35. Descent rate of the counter-rotating vortex pair (r_c/s' = 0.8)

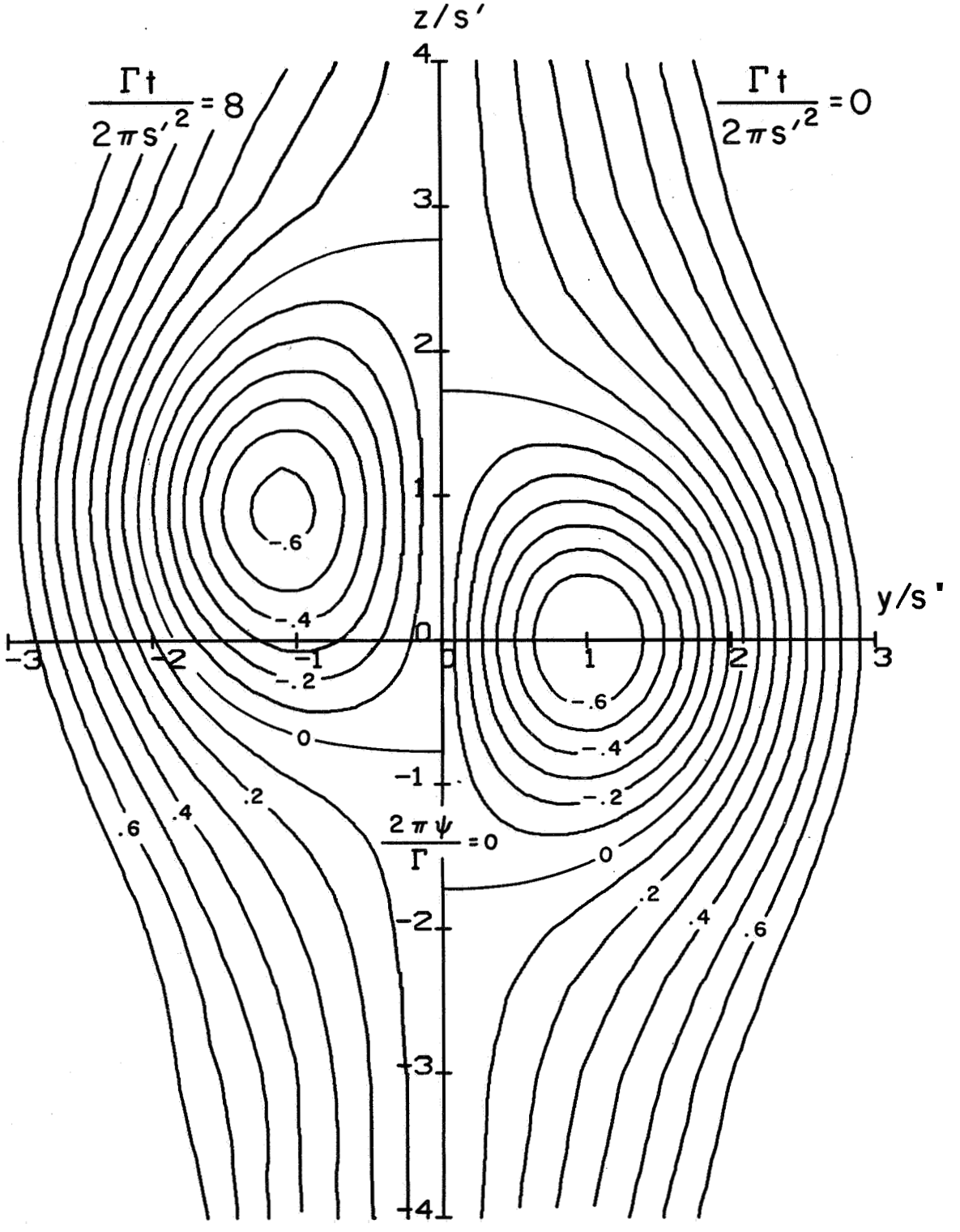

Figure 36. Instantaneous streamlines at $\Gamma t/2\pi s'^2 = 0.0$ and 8.0. The descent of the pair is stopped by adding an upwash of $\Gamma/4\pi s'$. Streamlines shown for $\Gamma t/2\pi s'^2 = 8.0$ have been reflected across the $y = 0$ axis.

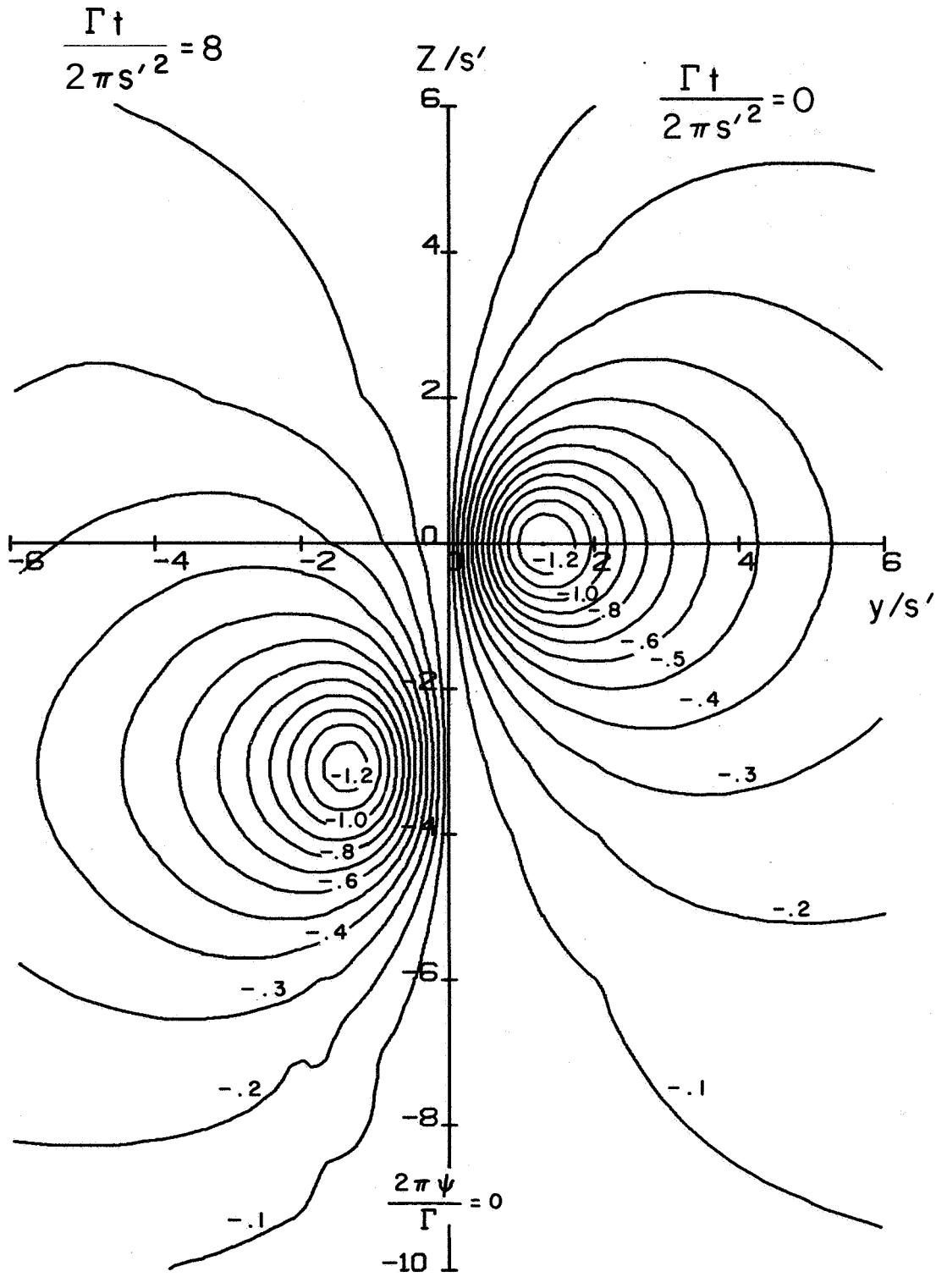

Figure 37. Instantaneous streamlines at $\Gamma t/2\pi s'^2$ = 0.0 and 8.0. The upwash added in Figure 36 has been removed and the pair permitted to descend. Streamlines shown for $\Gamma t/2\pi s'^2$ = 8.0 have been reflected across the y = 0 axis.

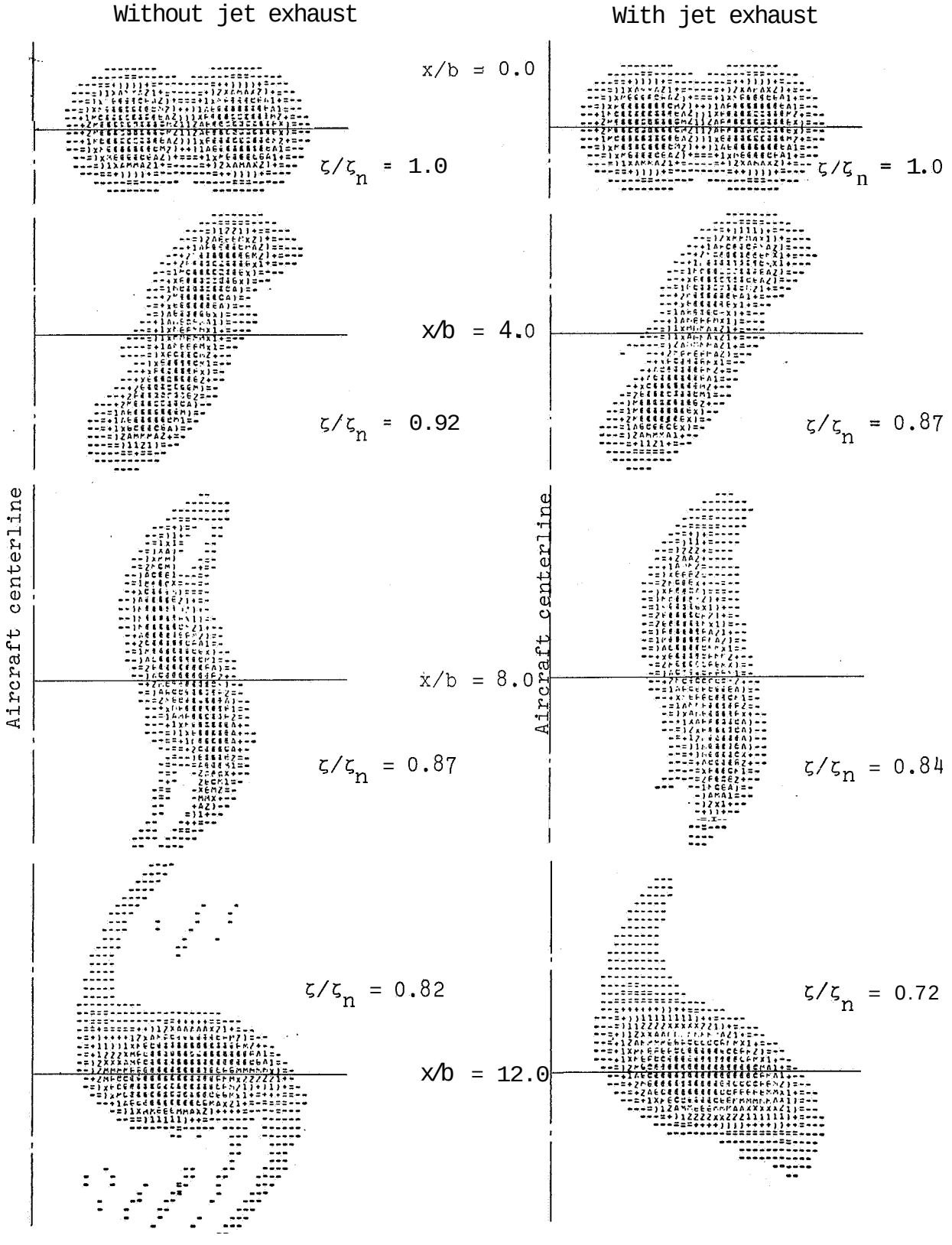

Figure 38. **Intensity** plots of **the** trailed vorticity ζ. $\zeta_n = 48.5\Gamma/2\pi s2$.

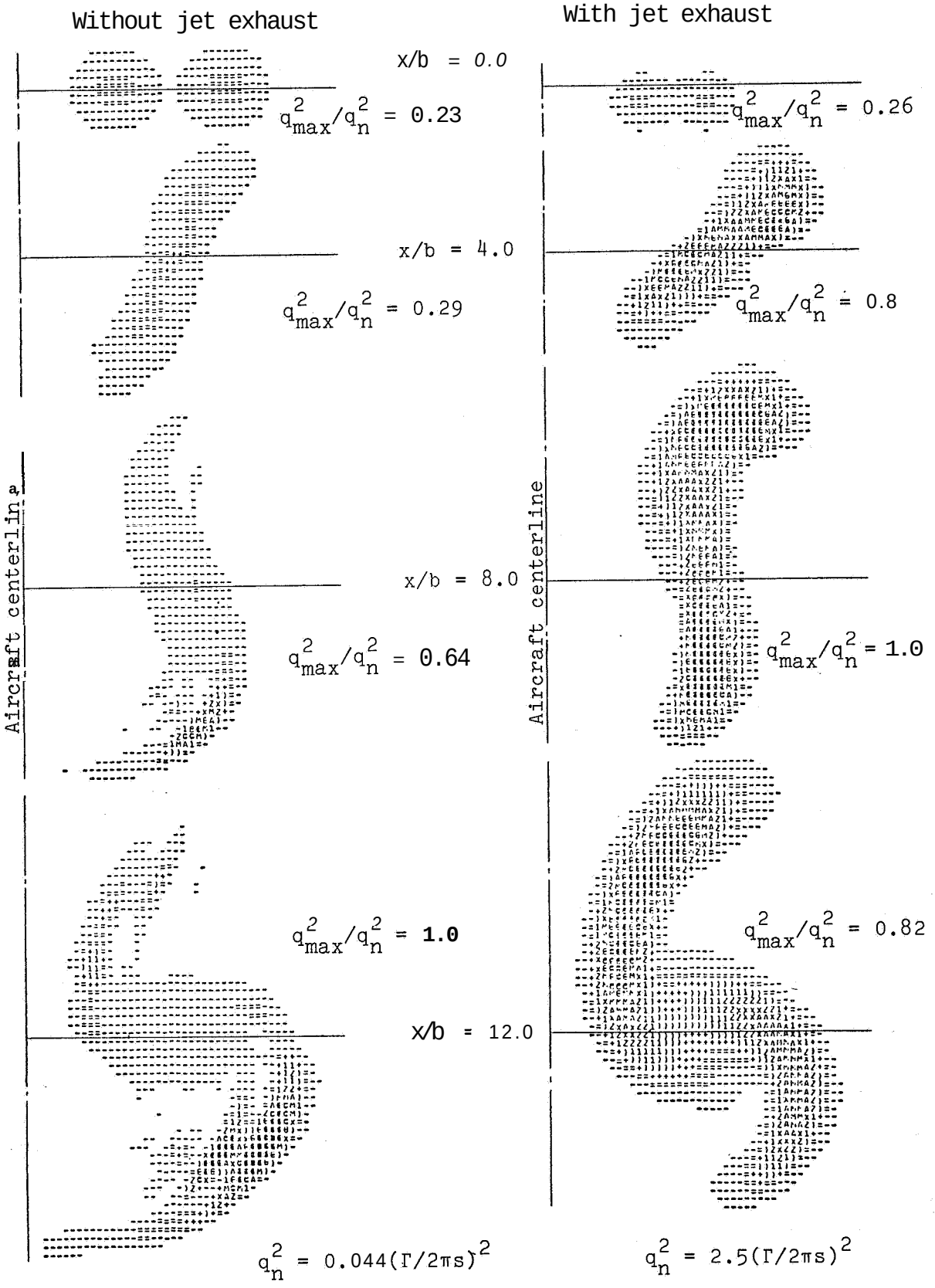

Figure 39. Intensity plots of the turbulent kinetic energy.

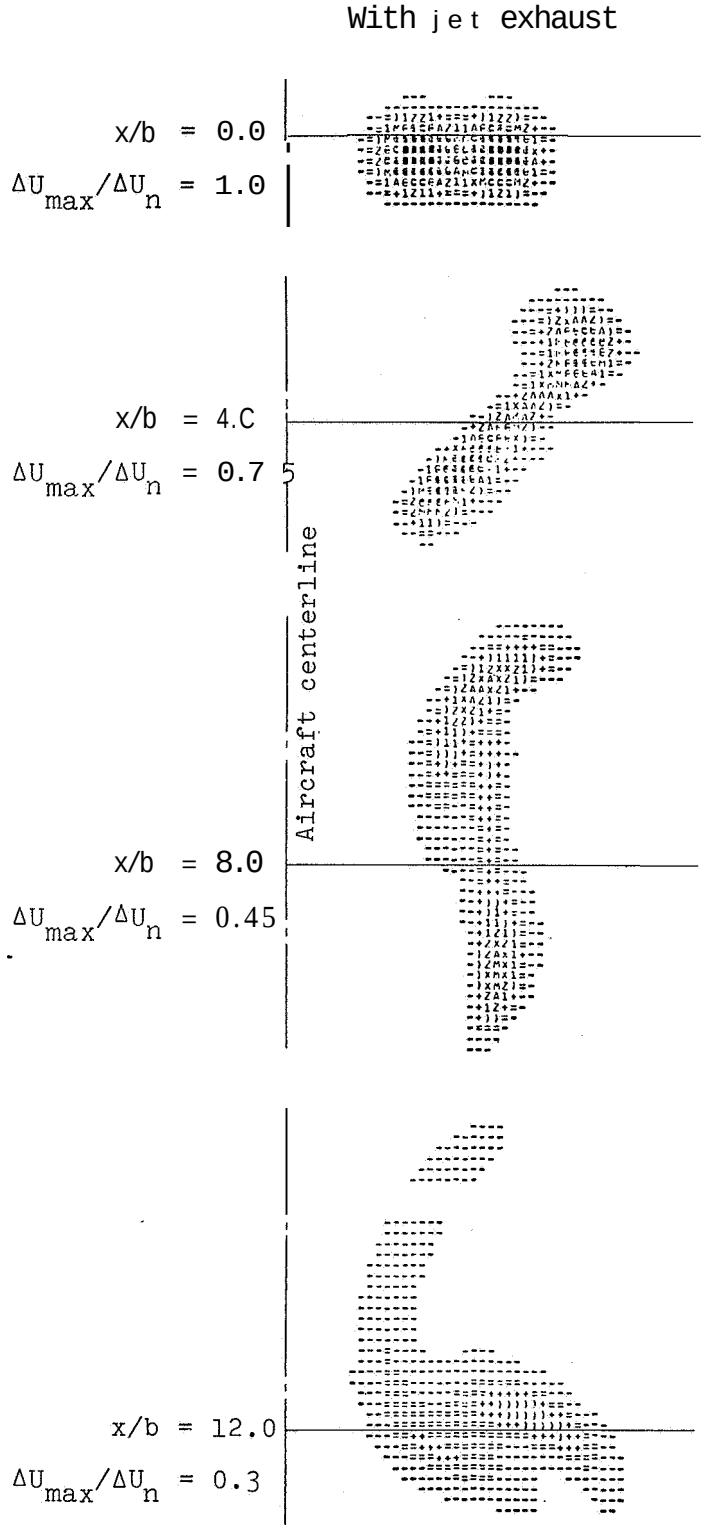

Figure 40. Intensity plots of the jet exhaust axial velocity excess. $\Delta U_n = 8.0\Gamma/2\pi s$.

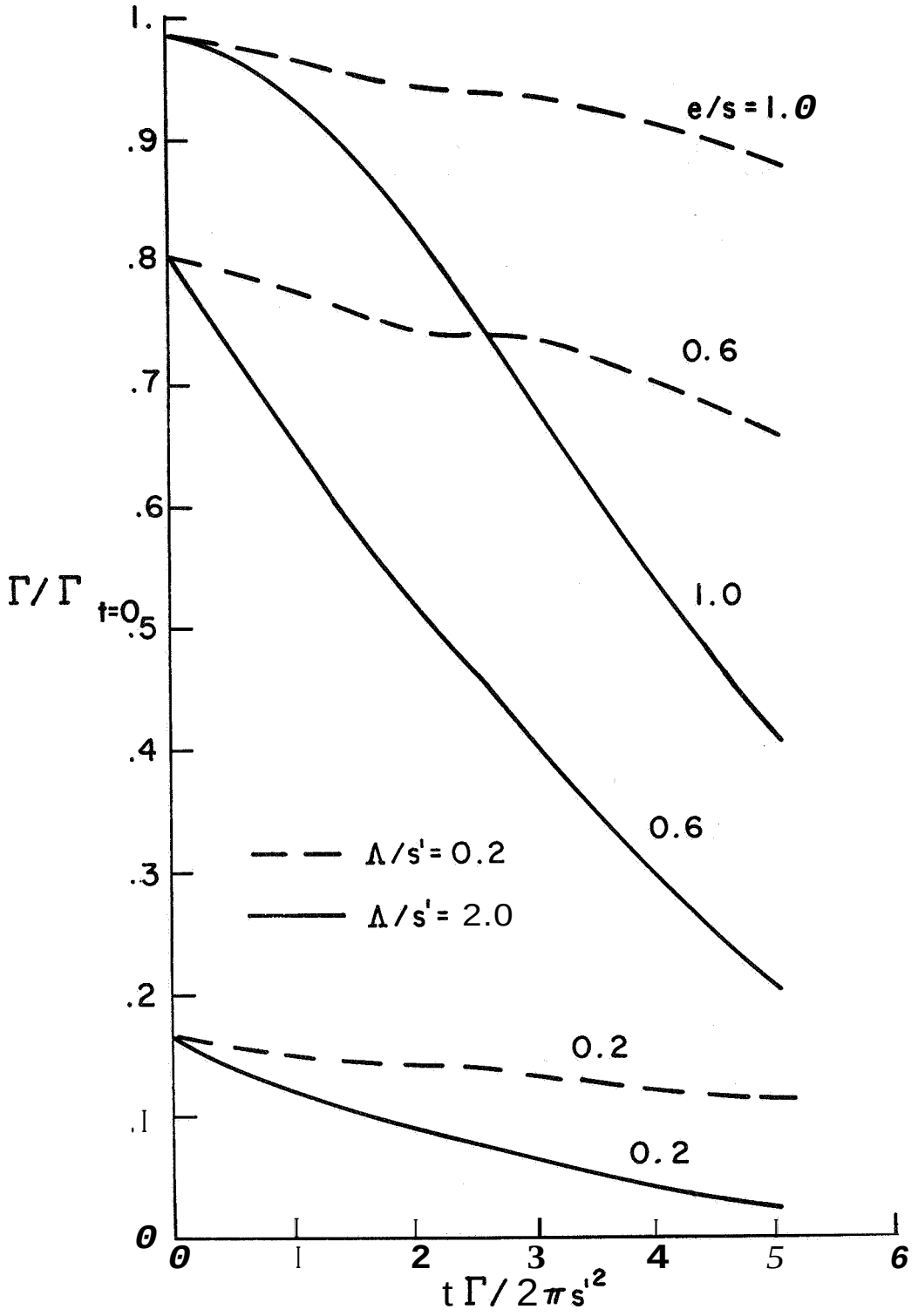

Figure 41. Decay of circulation in a counter-rotating vortex pair immersed in a turbulent atmosphere with constant turbulent dissipation rate ($\varepsilon^{1/3}$ = 2 $cm^{2/3}$/sec); see figure 34.